Detailed flow measurement of the field around tidal turbines with and without biomimetic leading-edge tubercles

Weichao Shi [1,2], Mehmet Atlar[2], Rosemary Norman[1]

1 School of Marine Science and Technology, Newcastle University, UK

2 Department of Naval Architecture, Ocean & Marine Engineering, University of Strathclyde, UK

Corresponding Author

Weichao Shi, w.shi6@ncl.ac.uk

School of Marine Science & Technology, Armstrong Building, Newcastle University
United Kingdom, NE1 7RU
Tel: 0044 (0)191 222 5067
Fax: 0044 (0)191 222 5491

Abstract: This paper focuses on implementing detailed flow measurement using advanced Particle Image Velocimetry (PIV) system to investigate the flow mechanism of leading-edge tubercles on tidal turbine blades. Two approaches have been applied: one is 2D PIV to map the flow separation around the blade sections at different radial positions; and the other is Stereo PIV to conduct a volumetric measurement in the wake field to reveal the tip vortex development and also velocity distribution. The research presented in this paper further demonstrates that the leading-edge tubercles can enable the flow to remain attached to the blades and weaken the three dimensional effect which can lead to efficiency loss or the so-called "tip loss". Based on these phenomena that have been observed and concluded from the tests, the mechanism by which leading-edge tubercles can provide additional torque and thrust for a tidal turbine has been explained within this paper.

Keywords: Particle Image Velocimetry (PIV), Tidal turbine, Blade design, Tubercles, Biomimetic

1 Introduction

Flow control devices have been widely adopted to stimulate the performance of foils and related devices; these include leading-edge slats, trail-edge flaps, winglets and vortex generators, etc. However recently a biomimetic concept, the leading-edge tubercles on the pectoral fins of humpback whales, has drawn attention [1, 2]. The tubercles first demonstrated a delayed stall and also enhanced lift-to-drag ratios in an investigation in wind tunnel tests for a pair of replica humpback whale flippers with and without leading-edge tubercles [3, 4]. Following this, investigations both numerical and experimental in nature, have looked at potential applications of leading-edge tubercles applied to air fans, wind turbines, rudders, propellers and so on [5-10].

Following a pioneering study that applied tubercles to a tidal turbine [11], recently the team in the Emerson Cavitation Tunnel (ECT), Newcastle University has initiated a new blade design study, by applying the concept to a tidal turbine [12-14]. Initially a study was conducted into a 3D hydrofoil with a tidal turbine chord length distribution but a constant pitch angle, which demonstrated the increased lift after the stall angle and the enhanced maximum lift-to-drag ratio [12]. Using computational fluid dynamics analysis, it was also shown that the three dimensional effect, which causes spanwise flow, can be reduced by the contra rotating vortex fence generated by the tubercles [15].

With confidence built from the hydrofoil study, the design was applied to a scaled turbine model with different levels of tubercle coverage. The scaled model tests were conducted for a number of different purposes, including hydrodynamic performance analysis, cavitation observation and noise performance. It has been proved that the hydrodynamic performance of the turbine can be enhanced in the low tip speed ratio region without lowering the maximum power coefficient, which will enable the turbine to start at lower flow velocities [13]. The tubercles can also help in restraining the cavitation region and hence lowering the noise level [14]. With these benefits, a quiet and quick reacting turbine design can be established.

However, the reasons why such benefits can be introduced by this tubercle concept have been discussed and argued by many researchers but not conclusively; these arguments include compartmentalization, vortex lift, varying the effective angle of attack and boundary layer momentum exchange [6]. Therefore, to further investigate the flow mechanism behind the tubercle function, a set of detailed flow measurements have been conducted. The test setup and results are presented and discussed in the following sections. Particle Image Velocimetry (PIV) technology was used to measure the velocity distribution and two different setups were employed, one for mapping of the flow separation and the other one for measuring the wake flow with 2D PIV and Stereo PIV (SPIV), respectively.

2 Description of the tested model

The reference turbine was chosen to be a model that was designed, tested and numerically modelled during a previous project [16, 17]. Based on this model, leading-edge tubercles were applied to the blades. The blade section of the reference turbine used the NREL S814 foil section, as shown in Figure 1. The main particulars for this 400mm diameter model turbine are shown in Table 1.

Three pitch-adjustable turbine models with different leading-edge profiles were manufactured by Centrum Techniki Okrętowej S.A. (CTO, Gdansk), as shown in Figure 2. “Ref” refers to the turbine model with a smooth leading edge; while “Sin2” refers to the one with two leading-edge tubercles at the tip; and the one with eight leading-edge tubercles is named “Sin8”. The sinusoidal leading-edge profile was developed as shown in Figure 3. The amplitude (A) of the sinusoidal tubercles was equal to 10% of the local chord length (C) while eight tubercles were evenly distributed along the radius with the wavelength (W) equal to 20mm. The profile of the leading tubercles was as represented by Equation 1.

$$H = \frac{A}{2} cos\left[\frac{2\pi}{W}(r - 40) - \pi\right] + \frac{A}{2}$$ Equation 1

Where H is the height of the leading-edge profile relative to the reference one which is the smooth leading-edge profile.

3 Experimental setup and approach

3.1 Description of the Emerson Cavitation Tunnel

The three tidal turbine models were tested in the Emerson Cavitation Tunnel (ECT) at Newcastle University. A sketch of the tunnel is shown in Figure 4. The tunnel is a medium size propeller cavitation tunnel with a measuring section of 1219mm × 806mm (width × height). The speed of the tunnel water varies between 0.5 and 8 m/s. Full details of the ECT can be found in [18].

3.2 Turbine control and force measurement

The turbine was mounted on a vertically driven dynamometer, Kempf & Remmers H33, designed to measure the thrust and torque of a propeller or turbine. A 64kW DC motor is mounted on top of the dynamometer to control the rotational speed of the turbine. The setup is shown in Figure 6.

The rotational speed is controlled by the motor to achieve the desired Tip Speed Ratio (TSR) which can be calculated using Equation 2. During the model tests, the torque and thrust of the turbine were measured and from these measurements the power coefficient (Cp) and the thrust coefficient (C_T) can be derived by using Equation 3 and Equation 4 respectively:

$$TSR = \frac{\omega r}{V}$$ Equation 2

$$Cp = \frac{Q\omega}{\frac{1}{2}\rho A_T V^3}$$ Equation 3

$$C_T = \frac{T}{\frac{1}{2}\rho A_T V^2}$$ Equation 4

where Q is the torque of the turbine, in Nm; T is the thrust, in N; ω is the rotational speed, in rad/s; A_T is the swept area of the turbine and equals $\pi D^2/4$, m^2; ρ is the tunnel water density, in kg/m^3; V is the incoming velocity, in m/s, D is the turbine diameter, in m.

As the performance of the turbine is strongly dependent on the Reynolds number and the cavitation number, these two non-dimensional numbers at 0.7 radius of the turbine blade, $Re_{0.7r}$ and $Cav_{0.7r}$ were monitored and can be derived from Equation 5 and Equation 6 respectively.

$$Re_{0.7r} = \frac{C_{0.7r}\sqrt{(V^2 + (0.7\omega r)^2}}{\nu}$$ Equation 5

$$Cav_{0.7r} = \frac{P_{0.7r} - P_v}{\frac{1}{2}\rho\sqrt{(V^2 + (0.7\omega r)^2}}$$ Equation 6

where $C_{0.7r}$ is the chord length of the turbine at 0.7 radius, m; ν is the kinematic viscosity of the water, m^2/s; $P_{0.7r}$ is the static pressure at the upper 0.7 radius of the turbine, Pa; P_v is the vapour pressure of the water, Pa.

Throughout the test campaign, the incoming flow velocity of the tunnel was fixed and the rotational speed was varied to achieve the required TSR. The tests were conducted according to the test matrix shown in Table 2. The test conditions are also shown in graphical format in Figure 5. At high Reynolds numbers, due to the increased incoming velocity, cavitation number was reduced and hence cavitation might occur at the turbine blades. Taking advantage of the pitch adjustable design, three different pitch angles of the turbine blades were tested. Details of the hydrodynamic performance, cavitation observation and noise measurement, have been presented in the papers [13, 14].

3.3 2D/ Stereo PIV system and calibration

The PIV system used in the ECT is a Dantec Dynamics Ltd system and a summary of its technical details is given in Table 3. In this test, both 2D PIV and SPIV measurements were conducted.

3.3.1 Setup of 2D PIV

Within this experiment, 2D PIV measurement was carried out for the purpose of measuring the velocity distribution within the planar sections at different radii, as shown in Figure 7. The two dimensional velocity vector in the plane can be measured in this way. The flow separation area can be mapped and compared after the test so that the differences of flow separation influenced by the leading-edge tubercles can be revealed.

The flow field was illuminated by the laser system and the highly seeded flow field was filmed using a high-speed CCD camera which was set perpendicular to the light sheet. A sample image is shown in Figure 8.

3.3.2 Setup of Stereo PIV

Following the 2D PIV measurement, a stereo PIV measurement was conducted to measure the three velocity components in a plane after the turbine. The measurement plane of the SPIV is shown in Figure 9.

The stereo PIV used the same laser system to illuminate the seeded flow field. However two high-speed cameras were used to capture the image from different angles. The setup of the Stereo PIV system in the ECT is shown in Figure 10. Typical images from the two cameras are shown in Figure 11.

The use of the SPIV needs special calibration for the two cameras, which involves a multi-level 270x190mm calibration target. In order to calibrate the SPIV system, the calibration target had to be installed in the measurement plane, as shown in Figure 12. The two cameras viewed the calibration target from the same side but different angles. The calibration result is shown in Figure 13, which also shows the camera positions.

3.4 Phase averaging and Image processing

Throughout the measurements of 2D PIV and stereo PIV, 100 double frame image pairs needed to be captured, analysed and averaged to achieve a time-averaged velocity distribution. In order to capture these images always at the same azimuth position of the turbine, the camera and the laser were controlled and synchronized by a cyclic synchronizer. This cyclic synchronizer is based on an encoder on the motor and a CompactDAQ system from National Instruments coded in LabVIEW, which has the capability of triggering the camera at the desired angular positions. However, the rotational rate of the turbine needed to have a minimum value of 350rpm to enable the system.

In order to analyse the images and hence to determine the flow velocities, adaptive PIV analysis was used for the 2D images from each camera. Afterwards, the results of these 100 velocity samples were averaged to achieve a final 2D PIV measurement. By combining the calibration results and the 2D PIV data, finally the SPIV results with three component velocity could be achieved, as shown in Figure 14, and also the detailed structure of the tip vortex could be revealed.

4 Testing conditions

Based on the hydrodynamic performance tests, the performance of the three turbines at three different pitch angles, 0^o, $+4^o$ and $+8^o$, was evaluated in the first stage, which provided the guidelines for the PIV measurement. According to the test result at 2m/s, shown in Figure 15 , even though $+8^o$ pitch angle has a slightly lower power coefficient (Cp) compared to $+4^o$, it has much lower thrust ($C_T/10$) and also a better starting performance in the lower range of TSRs. Therefore the $+8^o$ pitch angle was selected to be investigated in this paper for the PIV test.

The PIV test was conducted at three different TSRs in order to thoroughly understand the effect caused by the leading-edge tubercles while the turbine was operating under different conditions. This test needed to consider not only the minimum RPM requirement but also the impact of blade cavitation, since cavitation bubbles could greatly deteriorate the image quality. Therefore, the following three typical working conditions were selected.

1. Stall condition (TSR=2): Tidal turbine will experience this condition while accelerating up to the optimum working condition (TSR=4). However under this stall condition, flow separation could occur. The most significant improvement resulting from the leading-edge tubercles has been found under this condition. During the test, an incoming velocity of 4m/s and a rotational speed of 382rpm were used. The performance comparison of Cp and $C_T/10$ is presented in Table 4.

2. Optimum working condition (TSR=4): This is the optimum condition under which the turbine would operate in order to maximise the power generation. This is also the turbine’s design condition. Most turbines will maintain this TSR to achieve the maximum power coefficient. During the test, an incoming velocity of 3m/s and rotational speed of 573rpm were set.

3. Overspeed condition (TSR=5): This is the condition in which the turbine is working beyond the optimum TSR. This is often considered to be the overspeed condition that might be harmful for the generator and gearbox. However there are some turbines designed to operate under this condition since the higher rotational speed will result in better generator performance. More stable performance can be expected compared to the optimum working conditions under which the turbine might suffer from stall due to the natural flow fluctuation caused by waves or turbulence. During the test, an incoming velocity of 3m/s and rotational speed of 716rpm were set.

The performance comparison of the above three conditions has been summarised in Table 4. It can be noticed that at high TSR the increment in Cp for the turbine with tubercles is related to a rather significant increase in C_T. While at TSR=2, the increase in Cp is much higher than the increase in C_T, with the increase of TSR the inflow angle will be reduced inducing more thrust while with the decrease of TSR the opposite will be true for the inflow angle, i.e. increased inflow angle and hence more torque.

5 Result analysis

5.1 Visualizing the planar section using 2D PIV

For the purpose of mapping the flow separation region around the turbine blade, 2D PIV measurement was conducted for the above three turbines in the selected three typical conditions. All of the cases are referred to in the form "Model_Velocity_TSR_Position", i.e. "Ref_4_TSR2_0.95R".

The measurement result of 2D velocity distribution of the reference turbine at 0.95r under 4m/s with TSR=2 is presented in Figure 16 with the reference vector (U=4m/s, V=0m/s) displayed at the top left corner. It shows typical flow separation behind the turbine blades. However, in order to highlight the flow separation area behind the blade, the following results are presented in a form shown in Figure 17 with the reference vector being subtracted and the actual image being plotted in the background. As it can be seen, the turbine is suffering from significant flow separation after the blade, as marked between the white dashed lines. With this methodology, the flow separation area can be clearly mapped and compared.

All of the measurement results under TSR=2 are presented using the above method, as shown in Table 5. In order to clearly compare the flow separation area, the vorticity Z distribution is plotted in Table 6. In-depth analysis and a comparison between the performance of the three different turbines is shown in Table 4 indicating the dramatic difference in the stall condition, under which the flow around the turbine is also significantly changed by the tubercles. It can be clearly seen in Table 5 that the leading-edge tubercles can help the flow to be more attached to the turbine blade at various radial positions particularly from 0.8R to 0.95R. This phenomenon has proved the beneficial effect of the leading-edge tubercles for tidal turbines, especially under the stall condition is because of the more attached flow.

At sections towards the hub, the flow separation is gradually reduced due to the decreasing angle of attack. However the flow separation observed in the mid span region of the Sin8 turbine blades might be slightly larger from 0.6R to 0.45R as the result of the change in the angle of attack. This is because, at this region, the tubercles operating at unfavourable angles of attack and triggering a leading-edge flow separation due to the high speed flow induced by the tubercles. In contrast the reference turbine without tubercles will generate trailing-edge flow separation.

For the other two conditions, TSR=4 and TSR=5, the flow separation phenomenon has not been clearly observed since the angles of attack are lower than the stall angle; therefore the measurement results have been presented as a database for future research in Appendix A, Table 7 at TSR=4 and Table 8 at TSR=5.

5.2 Mapping the volumetric flow field using SPIV

By using SPIV, three velocity components: the axial velocity, the radial velocity and the tangential velocity can be visualised in the measuring plane downstream of the turbine blades along with the resultant vorticity distribution. With the aid of the phase locking and averaging technique discussed in Section 3.4, SPIV measurements were conducted every 10° of angular position and +/-5° within the blades themselves. Finally, by summarizing all of the data at different positions, a volumetric flow field can be achieved to resolve the turbine's wake field, as shown in Figure 18. In Figure 19 to Figure 27, the velocity magnitude distributions in the wake field downstream of these three different turbines under various conditions have been presented. In the following sections, detailed analysis and discussion are presented with regard to each of the individual conditions. Three sections, which are consecutively 50mm, 150mm and 250mm downstream of the turbine, were extracted and the velocity magnitude plotted at those sections.

5.2.1 Condition 1: Stall condition, TSR=2

In Figure 19 to Figure 21, the velocity magnitude distribution under the stall condition has been presented together with the iso-surface of axial velocity=1.5m/s. As discussed in Section 5.1, severe flow separation occurred under this condition. Because of the flow separation that the turbines suffered, in the wake field the flow is much more turbulent compared to the other conditions. Also, because of the low tip speed ratio, the tip vortex structure is not very clearly seen from the iso-surface.

It can be noticed that the tail of iso-surface plot for the Sin2 case is slightly behind the other two turbine cases and the associated iso-surface appears to be more intermittent compared to the other two cases and this results in a significant difference at section d=250mm. This is because of the fact that the flow is mixed quicker and hence the velocity deficit in the mid-span can be recovered faster by the Sin2 turbine compared to other two turbine cases. It can also be seen for section d=150mm the flow of Sin2 in the mid-span region has a higher speed compared to the other two turbine cases.

By extracting the iso-surface pair of radial velocity= +/-0.5m/s in Figure 28, the tip vortex can be revealed which is rolling from the pressure side to the suction side and disappearing in the wake. The iso-surface for the turbine Ref is wider and smoother than that for the other two turbines. For the case Sin8 especially, the iso-surface is quite narrow but extends for a longer distance. This trend can also be seen in which shows the iso-surface of the vorticity (tangential) = 100. This component of vorticity results from the axial velocity and the radial velocity and also reveals the tip vortex. As it can be seen, the iso-surface of the Sin8 case is longer but narrower. This indicates that the tip vortex of the turbines with tubercles under the stall condition is stronger but cannot influence as large an area of the blade because of the contra-rotating vortex fences created in between the tubercles. This phenomenon was also reported in a previous paper which claimed that these contra-rotating vortices generated by the tubercles help to reduce the blade from suffering further lift loss caused by the tip vortex [15].

On the other hand, some strong vortex development around 0.6R region can also be observed across the three turbines in Figure 29. This vortex development can be related to the flow separation in this region. At this TSR, the angles of attack along the radii varied significantly, which was also observed in the flow separation investigations, and hence resulting in difference of the vorticity distribution along the span.

5.2.2 Condition 2: Optimum working condition, TSR=4

In Figure 22 to Figure 24, the velocity magnitude distribution, while the turbines are operating at the optimum power coefficient condition, has been presented together with the iso-surface of axial velocity=3.3m/s. The iso-surfaces in these plots reveal the classic structure of the tip vortex. By comparing these iso-surfaces, it can be seen that the strength of these tip vortices is gradually weakened by the tubercles as the iso-surface gradually gets shorter with the increase in the number of tubercles.

On the other hand, the velocity deficit behind the turbine increases with the numbers of tubercles, as it can be seen in the section plots. This is due to the higher induction factor that is generated by the turbine with tubercles. This can also be seen in Table 4 where the force measurement, represented by the thrust coefficient, is 4.6% and 7.7% higher for the Sin2 and Sin8 cases, respectively, relative to the reference turbine and the power coefficient is similarly 2.2% and 4.3% higher.

5.2.3 Condition 3: Overspeed condition, TSR=5

A similar trend to Condition 2 can also be observed in Condition 3 in Figure 25 to Figure 27, where the turbine is working under the overspeed condition. The iso-surface also gradually shortens with the increase in the number of tubercles, which shows the weakened tip vortex resulting from the tubercles. The same trend is also seen in terms of the increased velocity deficit from the tubercles and this is even more pronounced compared to Condition 2; the thrust coefficient being 4.0% and 9.2% higher and the power coefficient 1.6% and 4.0% higher for the Sin2 and Sin8 cases compared to the reference turbine, as seen in Table 4.

6 Conclusions

Following on from the previous experimental studies of the hydrodynamic performance and the cavitation and noise performance of tidal turbines with biomimetic leading-edge tubercle designs, this paper focuses on detailed flow measurement using both 2D PIV and stereo PIV in order to investigate the flow mechanisms around the turbine with the assumption of steady flow.

The measurements were conducted in three typical operating conditions: 1. Stall condition (TSR=2), 2. Optimum working condition (TSR=4) and 3. Overspeed condition (TSR=5), and the findings have been concluded as follows:

1. With the aid of 2D PIV, the flow separation around the blade sections at every 10 mm radius has been mapped and compared under all of the selected conditions. Under the Stall condition, while all turbine blades suffer from severe flow separation, the turbines with leading-edge tubercles can help to maintain the flow to be more attached to the blade surface at certain positions, which provides the turbine additional torque for starting. In the other two conditions, since the flow does not separate from the blades, there is no clear difference seen.

2. By using SPIV, a volumetric measurement has been conducted and the flow structure in the wake field with three velocity components has been obtained. This reveals the flow structure downstream of the turbine. It can be clearly seen that turbines with tubercles can induce a higher induction factor, which results in lower velocity in the wake field and higher power and thrust coefficients. This effect is positively related to the number of tubercles.

3. Also it can be noticed in the SPIV measurement that the tip vortex can be weakened and its axial trajectory is shortened by the tubercles in the optimum working condition and the overspeed condition. Therefore, the three dimensional effect can be reduced by the tubercles. Under the stall condition, the tubercles help the turbine to confine the vortex at the tip region and isolate it from influencing larger areas of the blades which also weakens the three dimensional effect.

One should be born in mind that the study presented in this paper and resulting conclusions are based on the steady state experimental investigations conducted at the model scale and analyses of the associated data. However, in real world with the full-scale applications, the important issue of the scale effect and that of the unsteady or transient flow effects (e.g. stall and over speeding) will require further investigations for the through exploitation of the tubercle applications on tidal turbine blades."

Acknowledgement

This research is funded by the School of Marine Science and Technology, Newcastle University and the China Scholarship Council. The financial support obtained from both establishments is gratefully acknowledged. The Authors would also like to thank all the team members in the Emerson Cavitation Tunnel for their help in testing and sharing their knowledge.

Reference

[1] F.E. Fish, J.M. Battle, Hydrodynamic design of the humpback whale flipper, Journal of Morphology 225:51-60 (1996).

[2] F.E. Fish, P.W. Weber, M.M. Murray, L.E. Howle, The tubercles on humpback whales' flippers: application of bio-inspired technology, Integrative and comparative biology 51(1) (2011) 203-13.

[3] D.S. Miklosovic, M.M. Murray, L.E. Howle, Experimental evaluation of sinusoidal leading edges, J Aircraft 44(4) (2007) 1404-1408.

[4] D.S. Miklosovic, M.M. Murray, L.E. Howle, F.E. Fish, Leading-edge tubercles delay stall on humpback whale (Megaptera novaeangliae) flippers, Phys Fluids 16(5) (2004) L39-L42.

[5] I.H. Ibrahim, T.H. New, Tubercle modifications in marine propeller blades, 10th Pacific Symposium on Flow Visualization and Image Processing, Naples, Italy, 2015.

[6] M.D. Bolzon, R.M. Kelso, M. Arjomandi, Tubercles and Their Applications, Journal of Aerospace Engineering 29(1) (2016) 04015013.

[7] P.W. Weber, L.E. Howle, M.M. Murray, Lift, Drag, and Cavitation Onset On Rudders With Leading-edge Tubercles, Mar Technol Sname N 47(1) (2010) 27-36.

[8] M.J. Stanway, Hydrodynamic effects of leading-edge tubercles on control surfaces and in flapping foil propulsion, Department of Mechanical Engineering, Massachusetts Institute of Technology, 2008.

[9] L.E. Howle, Whalepower wenvor blade, Bellequant Engineering, PLLC, 2009.

[10] A. Corsini, G. Delibra, A.G. Sheard, On the Role of Leading-Edge Bumps in the Control of Stall Onset in Axial Fan Blades, J Fluid Eng-T Asme 135(8) (2013) 081104-081104.

[11] T. Gruber, M.M. Murray, D.W. Fredriksson, Effect of humpback whale inspired tubercles on marine tidal turbine blades, ASME 2011 International Mechanical Engineering Congress and Exposition, American Society of Mechanical Engineers, 2011, pp. 851-857.

[12] W. Shi, M. Atlar, R. Norman, B. Aktas, S. Turkmen, Numerical optimization and experimental validation for a tidal turbine blade with leading-edge tubercles, Renewable Energy 96 (2016) 42-55.

[13] W. Shi, R. Rosli, M. Atlar, R. Norman, D. Wang, W. Yang, Hydrodynamic performance evaluation of a tidal turbine with leading-edge tubercles, Ocean Engineering 117 (2016) 246-253.

[14] W. Shi, M. Atlar, R. Rosli, B. Aktas, R. Norman, Cavitation observations and noise measurements of horizontal axis tidal turbines with biomimetic blade leading-edge designs, Ocean Engineering 121 (2016) 143-155.

[15] W. Shi, M. Atlar, K. Seo, R. Norman, R. Rosli, Numerical simulation of a tidal turbine based hydrofoil with leading-edge tubercles, 35th International Conference on Ocean, Offshore and Arctic Engineering, OMAE2016, Proceedings of the ASME 2016, Busan, Korea, 2016.

[16] D. Wang, M. Atlar, R. Sampson, An experimental investigation on cavitation, noise, and slipstream characteristics of ocean stream turbines, P I Mech Eng a-J Pow 221(A2) (2007) 219-231.

[17] W. Shi, D. Wang, M. Atlar, K.-c. Seo, Flow separation impacts on the hydrodynamic performance analysis of a marine current turbine using CFD, Proceedings of the Institution of Mechanical Engineers, Part A: Journal of Power and Energy 227(8) (2013) 833–846.

[18] M. Atlar, Recent upgrading of marine testing facilities at Newcastle University, AMT'11, Newcastle upon Tyne, UK, 2011, pp. 4-6.

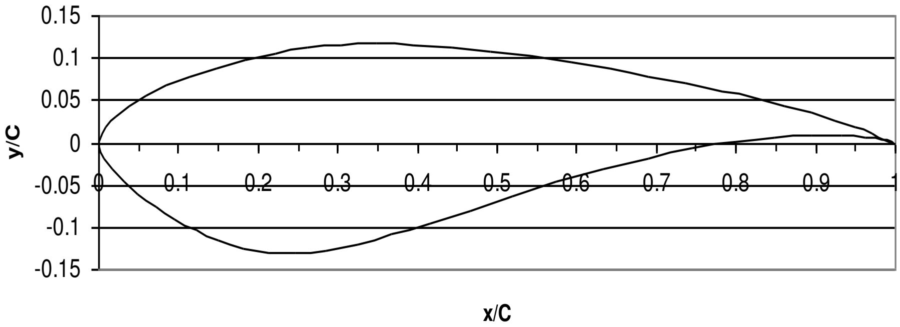

Figure 1. S814 foil section

Figure 2. Tested turbine models

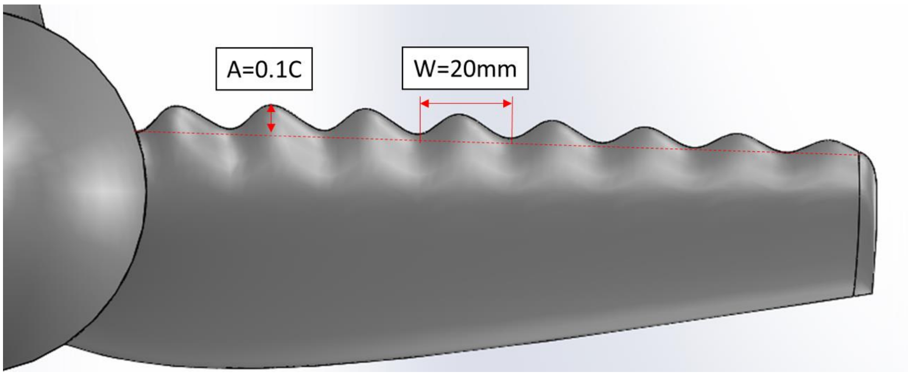

Figure 3. 3D design of the turbine blade with leading-edge tubercles

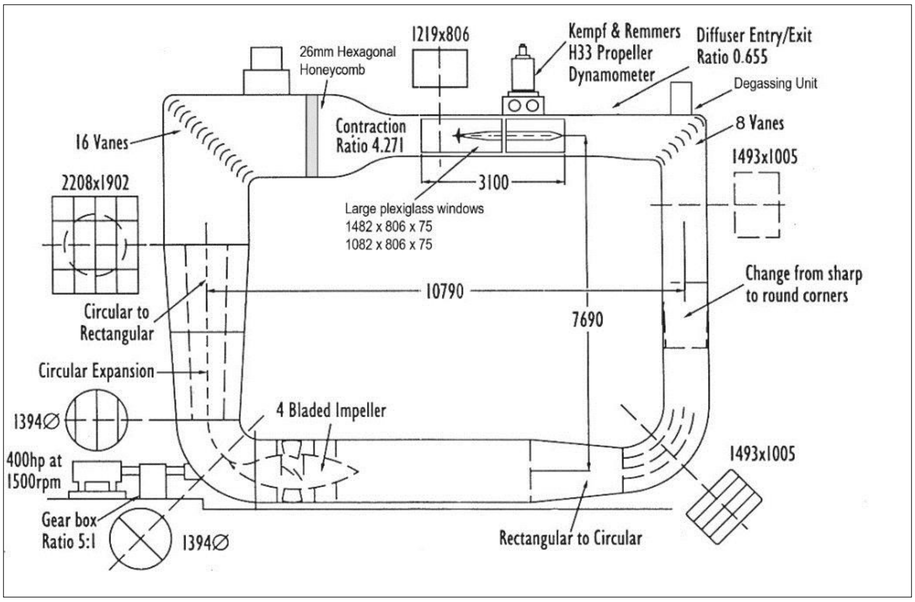

Figure 4. Sketch of Emerson Cavitation Tunnel

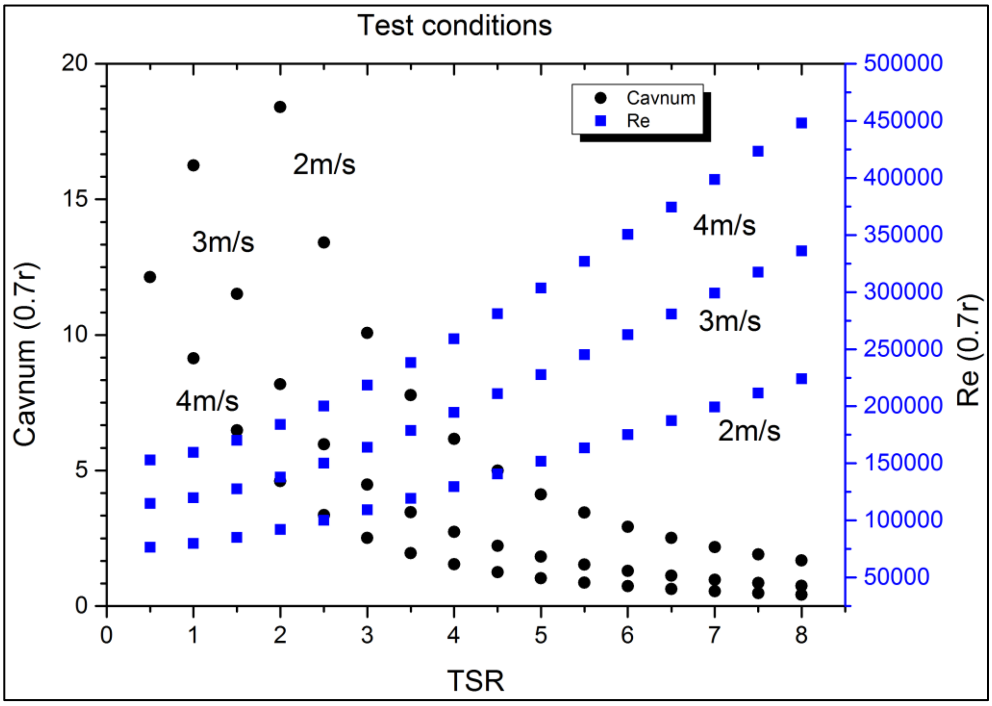

Figure 5 Test conditions

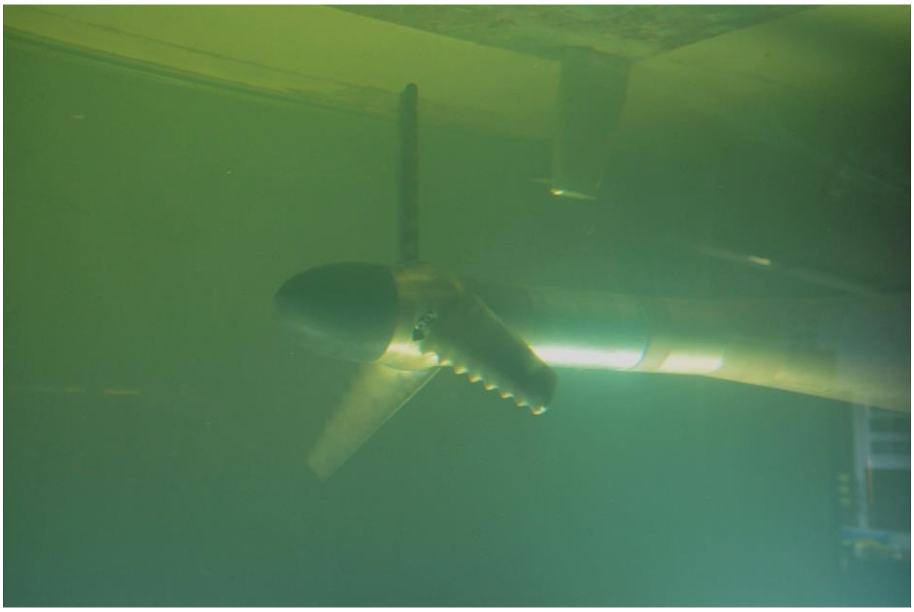

Figure 6. Model turbine mounted on the dynamometer and being tested in Emerson Cavitation Tunnel

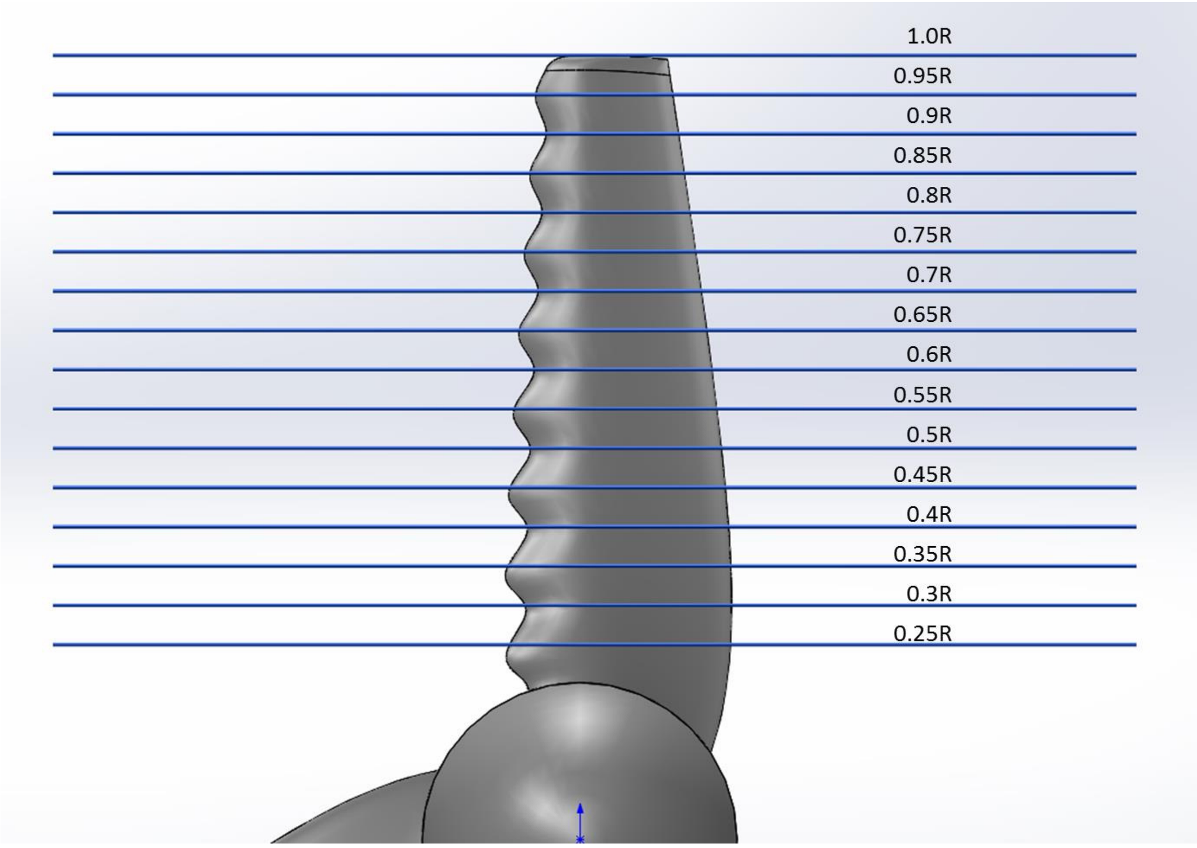

Figure 7. Radial positions of 2D PIV measurement planes

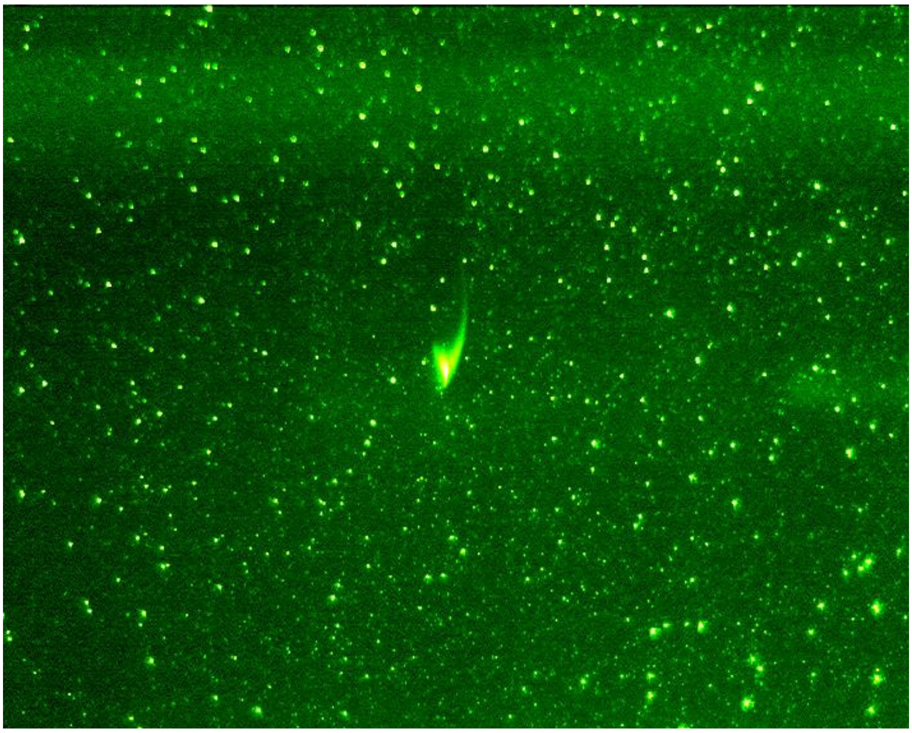

Figure 8. Sample image of 2D PIV

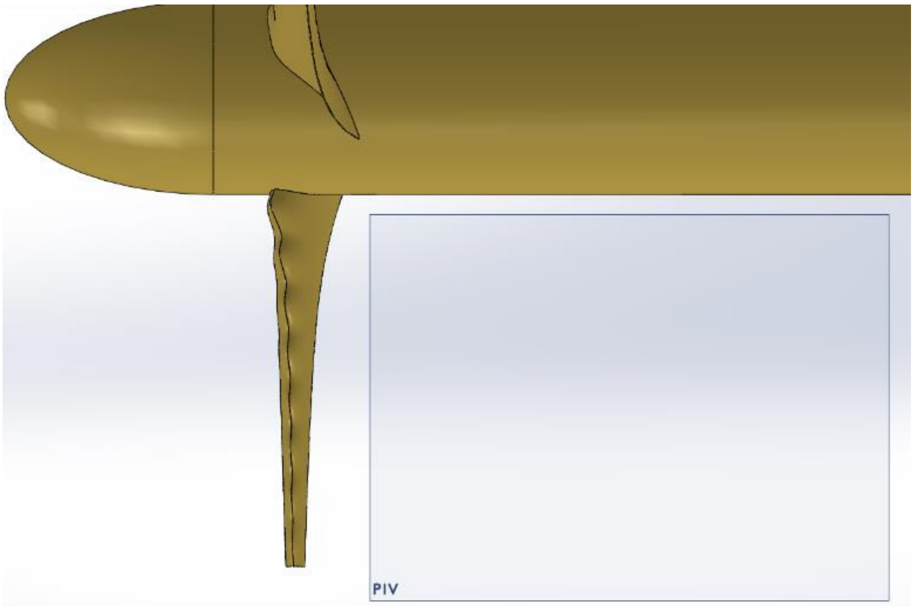

Figure 9. Stereo PIV measurement plane

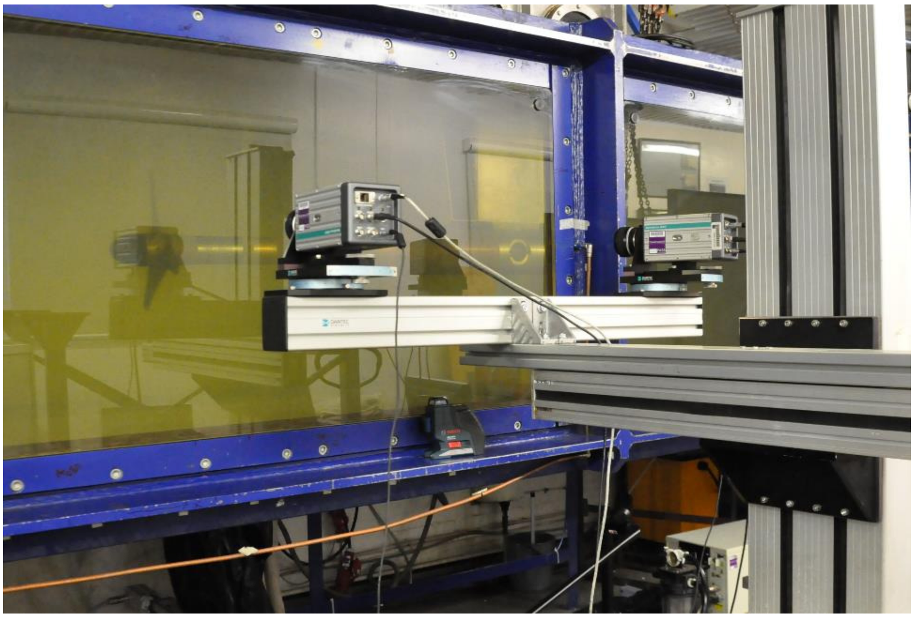

Figure 10. Setup of Stereo PIV alongside the test section of Emerson Cavitation Tunnel

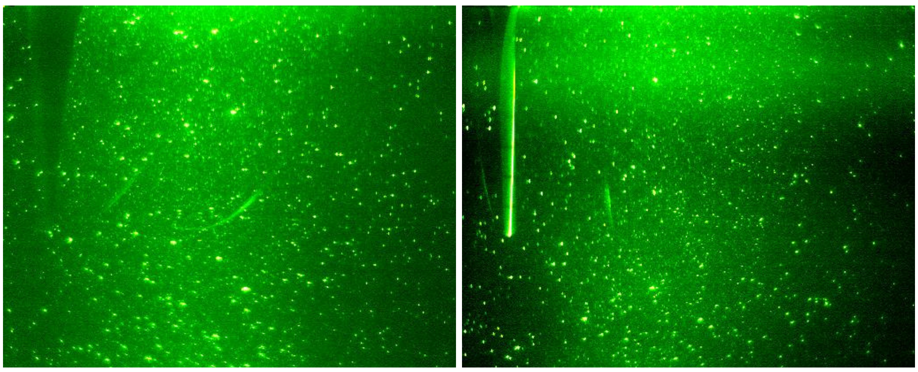

Figure 11. Typical stereo PIV Images from two different cameras shooting from different perspective angles

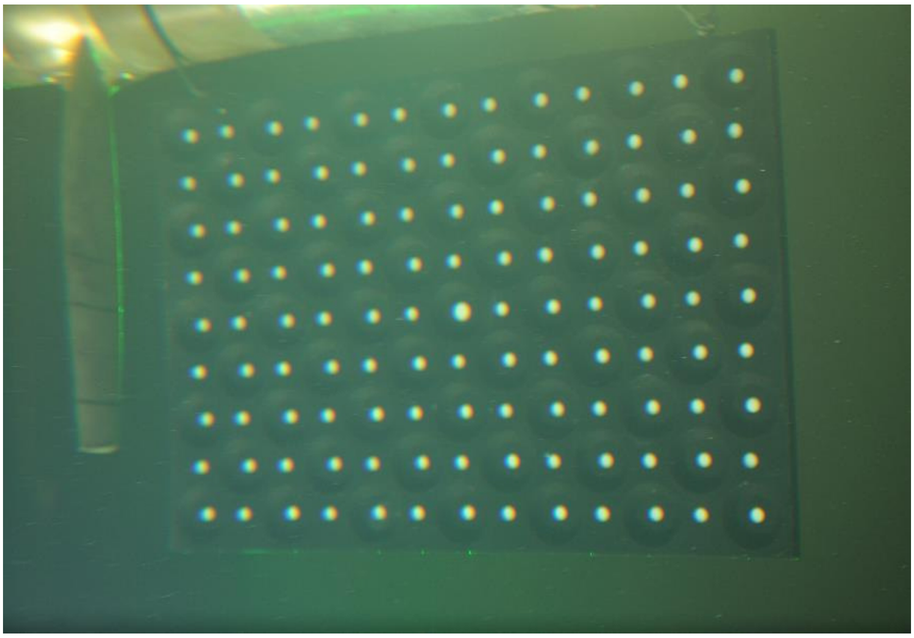

Figure 12. Calibration target for stereo PIV system located at downstream of model turbine

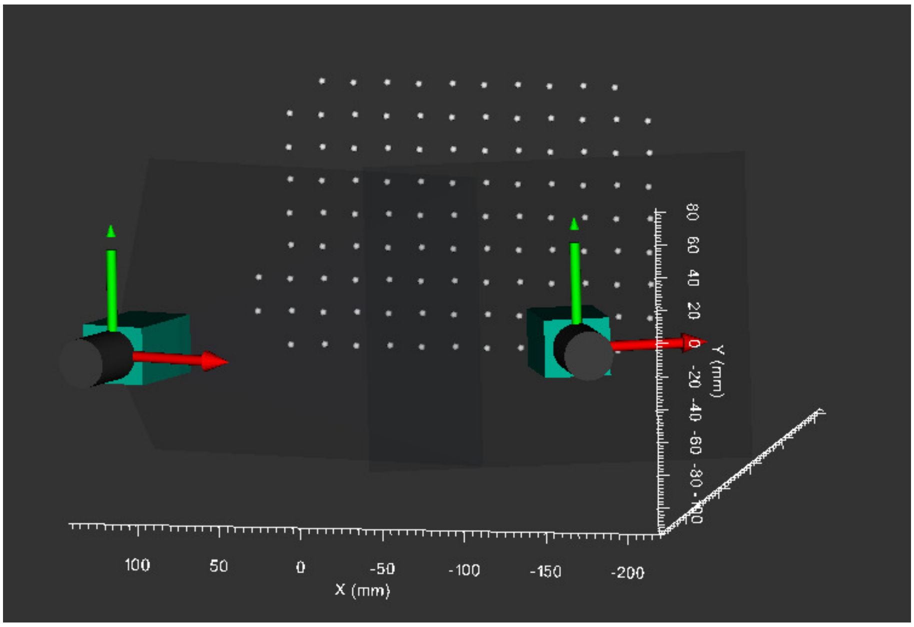

Figure 13. Calibration result of stereo PIV

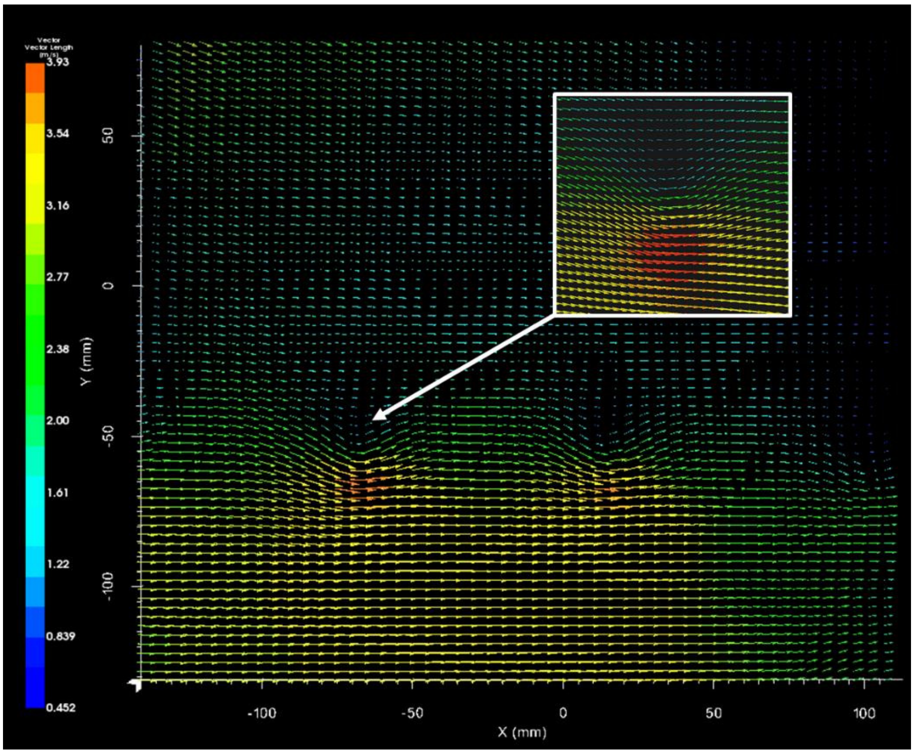

Figure 14. Stereo PIV result with a detailed tip vortex structure

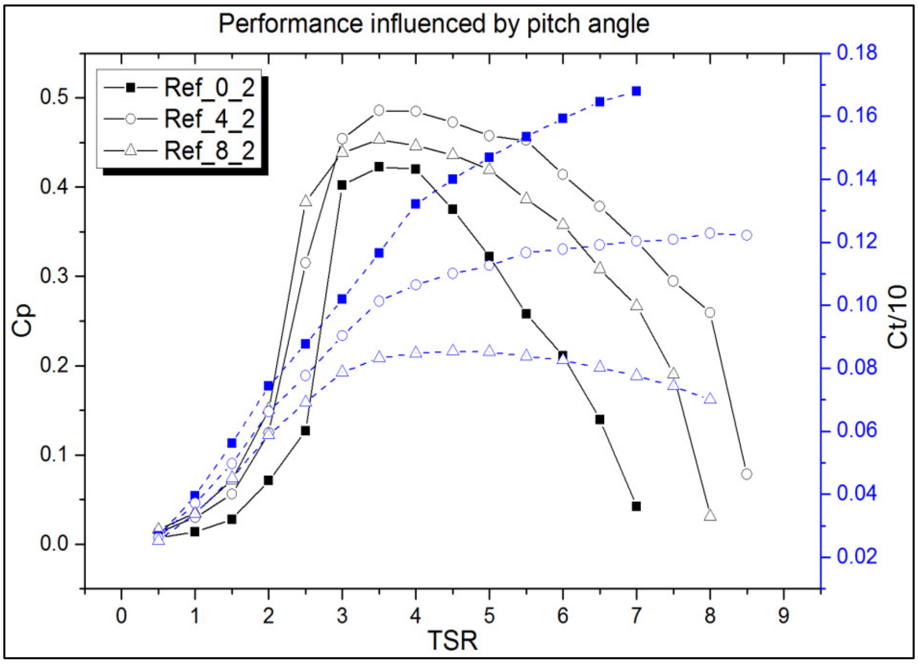

Figure 15. Performance of Reference turbine in terms of power (Cp) and thrust (C_T) coefficients for different pitch settings

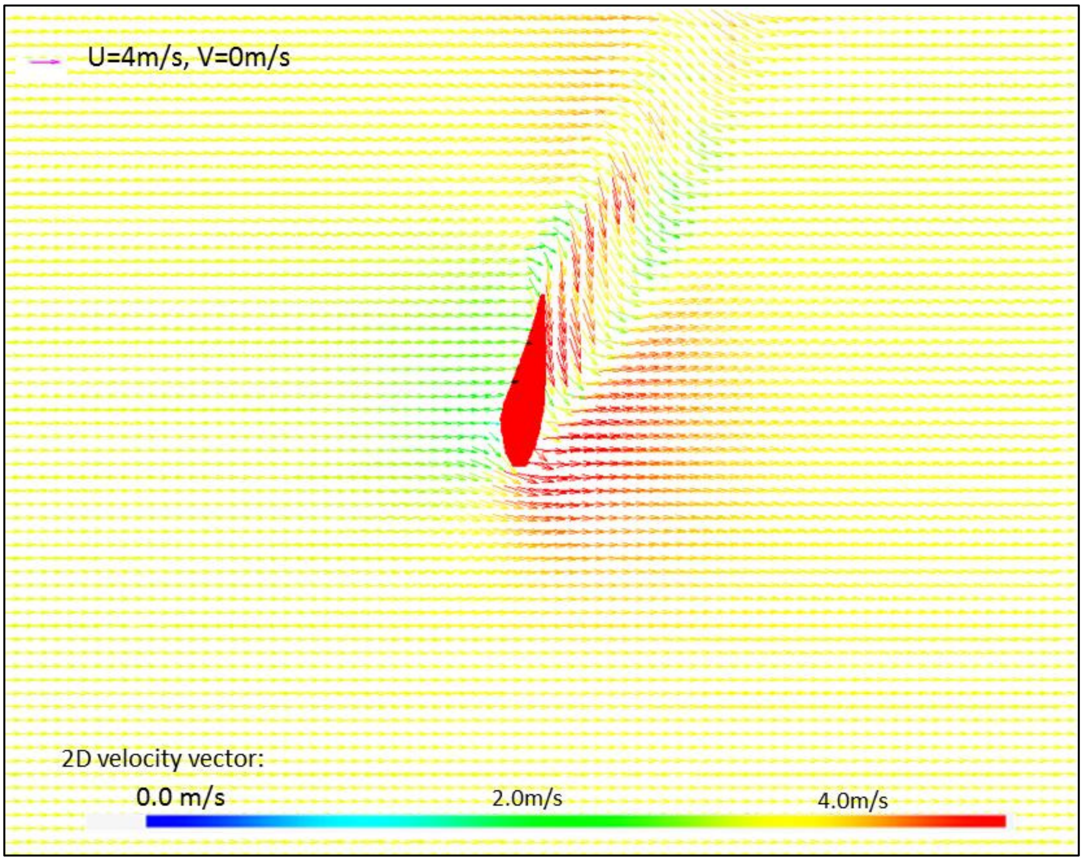

Figure 16. Velocity distribution of turbine blade section by using 2D PIV (Case: Ref_4_TSR2_0.95R)

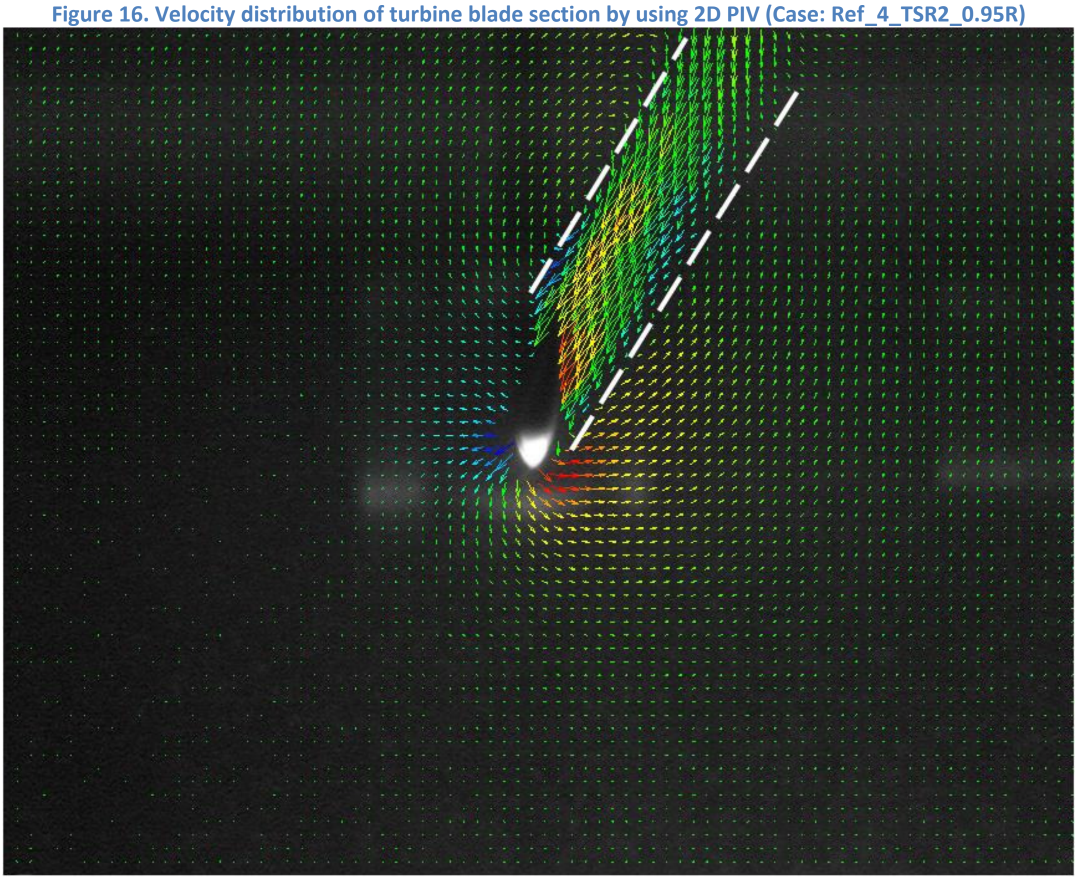

Figure 17. Mapping of flow separation area in downstream of turbine blade by using 2D PIV (Case: Ref_4_TSR2_0.95R)

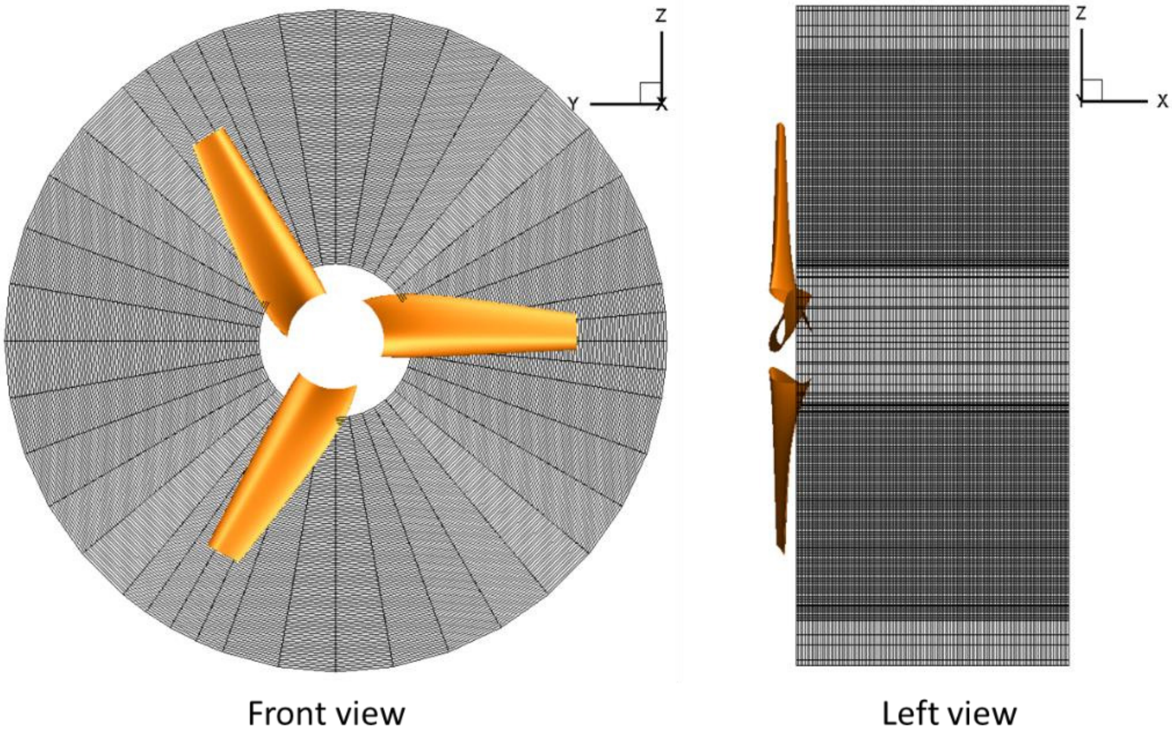

Figure 18. Volumetric flow field description for stereo PIV measurements

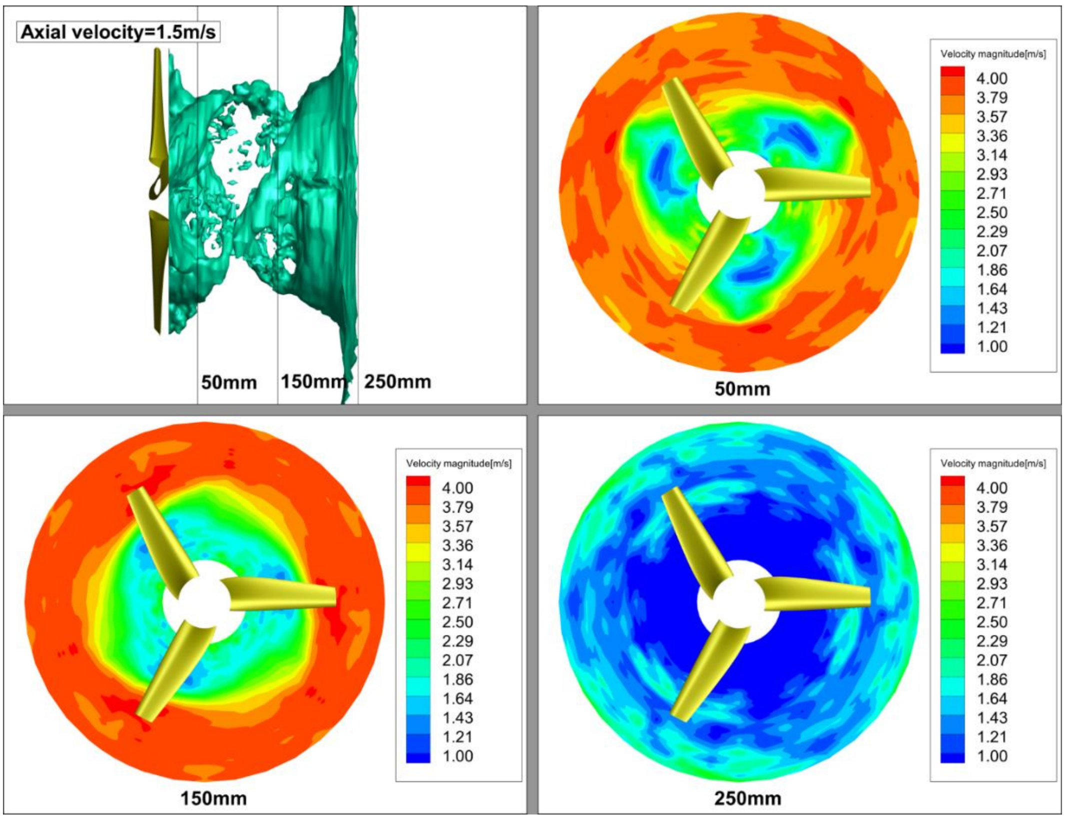

Figure 19. Velocity magnitude distribution for the reference turbine at varied sections, 50mm, 150mm and 250mm downstream of model turbine at TSR2 with the iso-surface of axial velocity = 1.5m/s

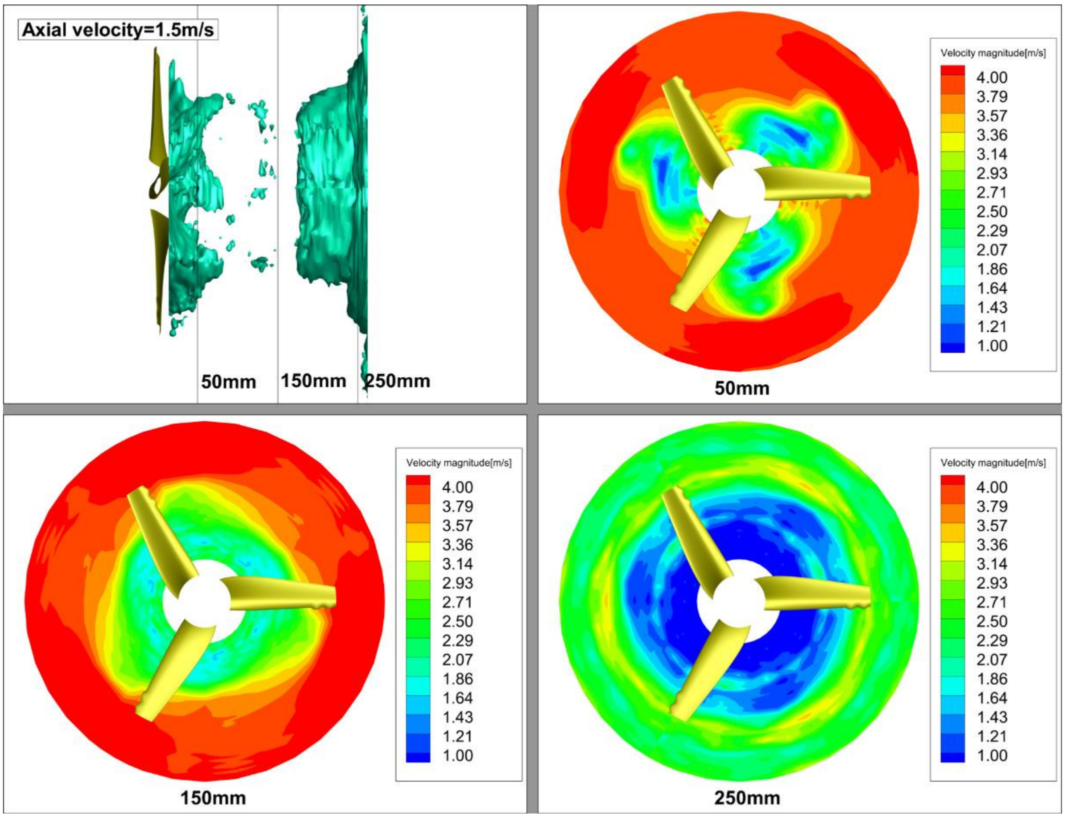

Figure 20 Velocity magnitude distribution for the Sin2 turbine at varied sections, 50mm, 150mm and 250mm downstream of model turbine at TSR2 with the iso-surface of axial velocity = 1.5m/s

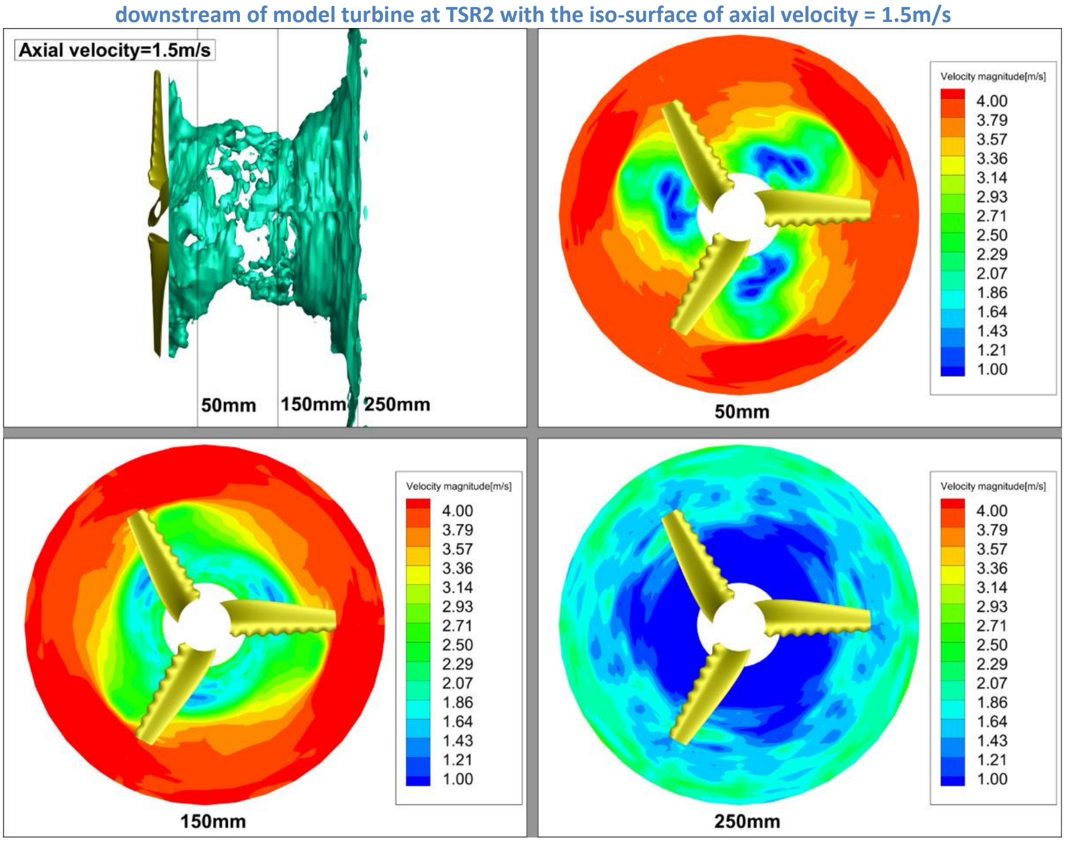

Figure 21. Velocity magnitude distribution for the Sin8 turbine at varied sections, 50mm, 150mm and 250mm downstream of model turbine at TSR2 with the iso-surface of axial velocity = 1.5m/s

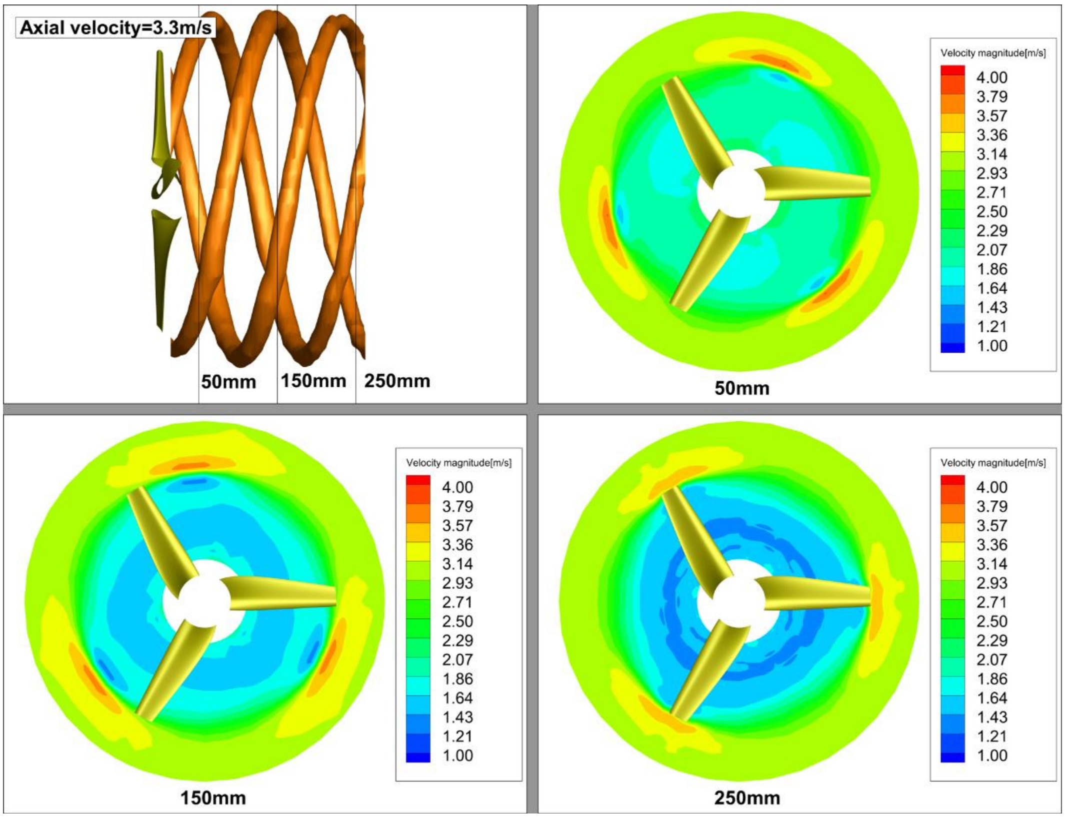

Figure 22. Velocity magnitude distribution for the reference turbine at varied sections, 50mm, 150mm and 250mm downstream of model turbine at TSR4 with the iso-surface of axial velocity = 3.3m/s

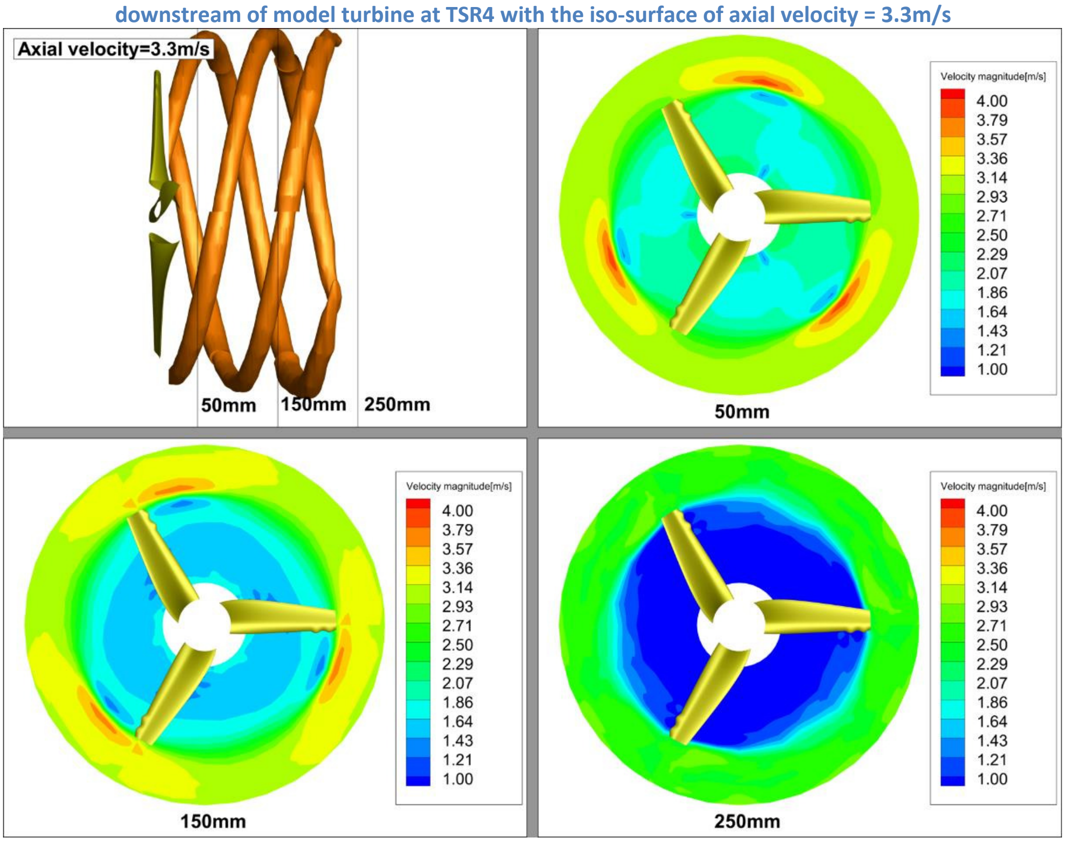

Figure 23. Velocity magnitude distribution for the Sin2 turbine at varied sections, 50mm, 150mm and 250mm downstream of model turbine at TSR4 with the iso-surface of axial velocity = 3.3m/s

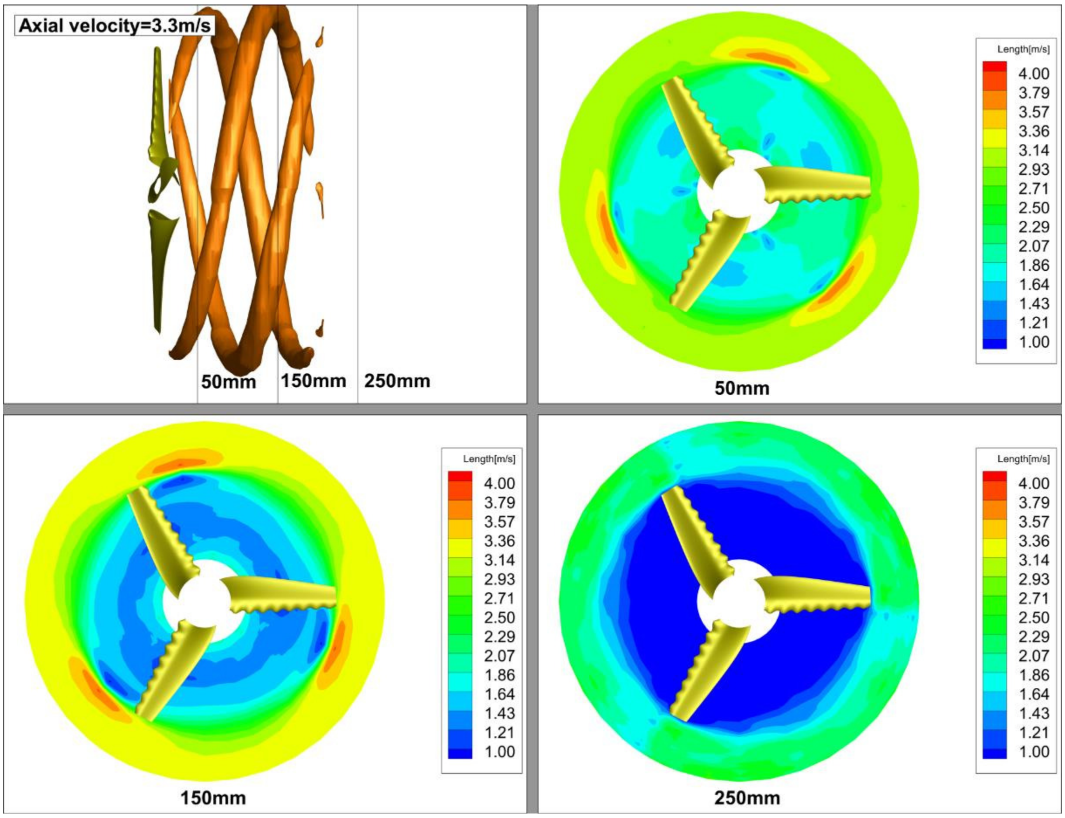

Figure 24. Velocity magnitude distribution for the Sin8 turbine at varied sections, 50mm, 150mm and 250mm downstream of model turbine at TSR4 with the iso-surface of axial velocity = 3.3m/s

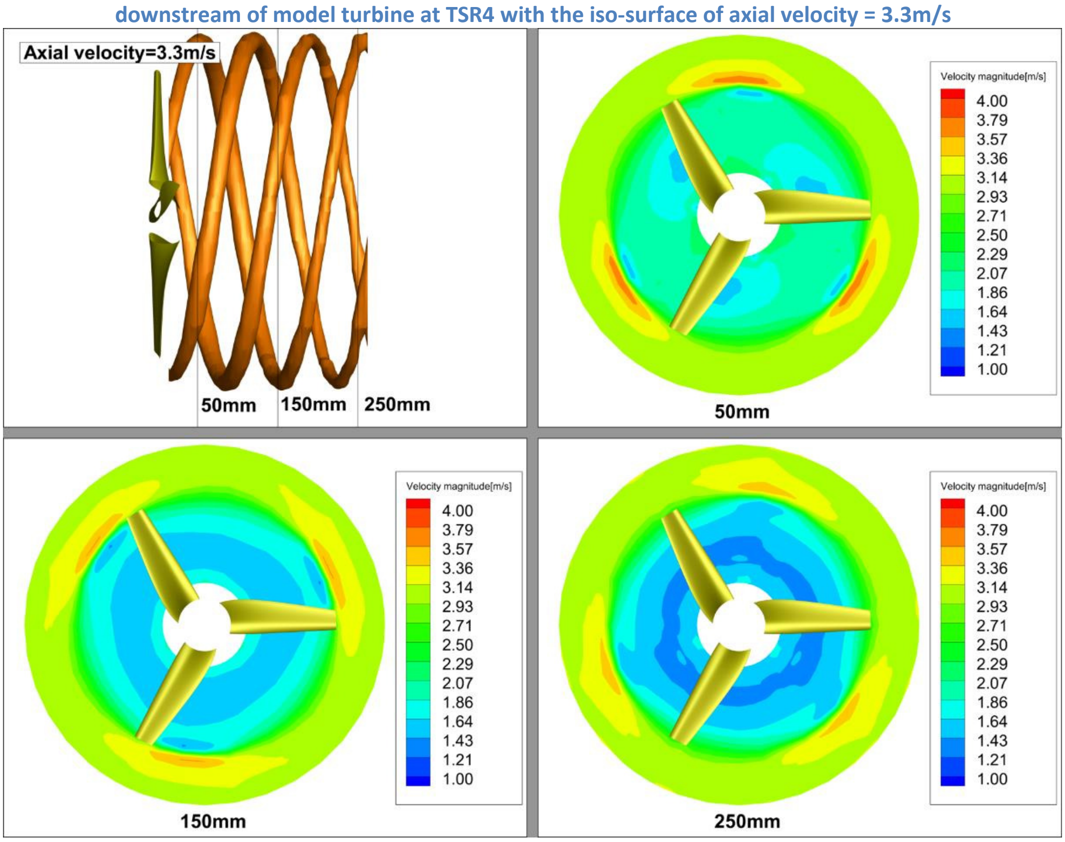

Figure 25. Velocity magnitude distribution for the reference turbine at varied sections, 50mm, 150mm and 250mm downstream of model turbine at TSR5 with the iso-surface of axial velocity = 3.3m/s

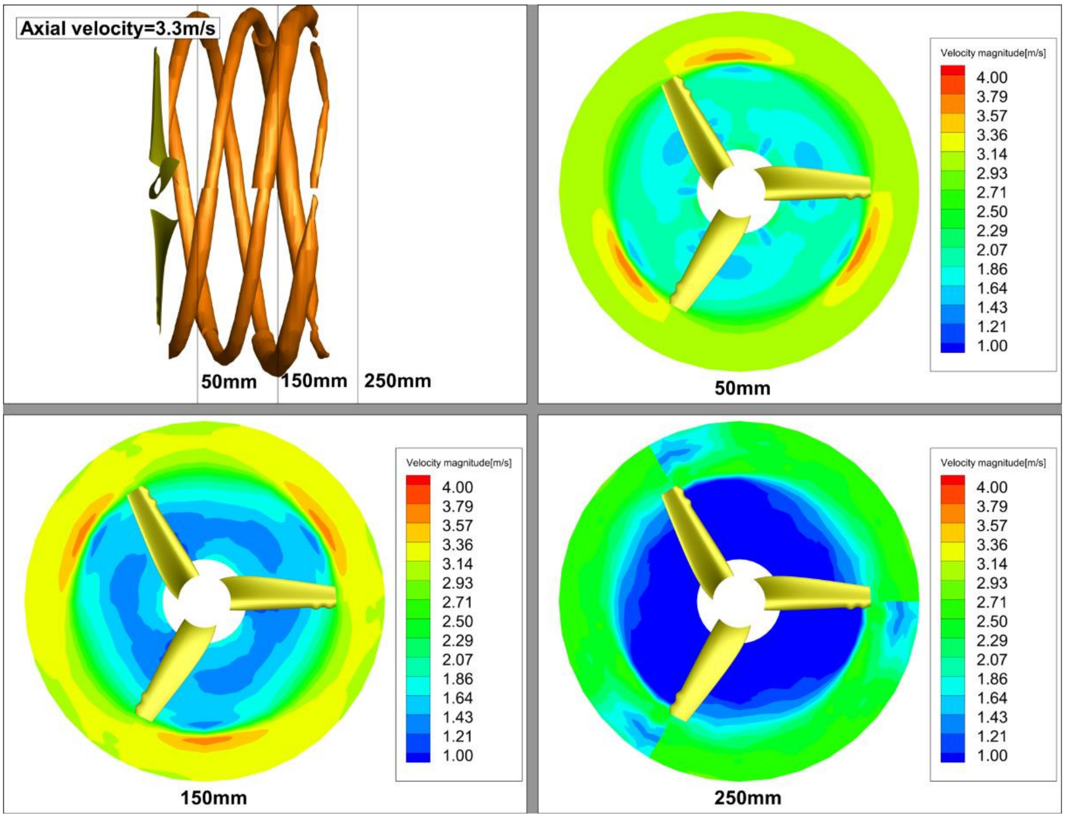

Figure 26. Velocity magnitude distribution for the Sin2 turbine at varied sections, 50mm, 150mm and 250mm downstream of model turbine at TSR5 with the iso-surface of axial velocity = 3.3m/s

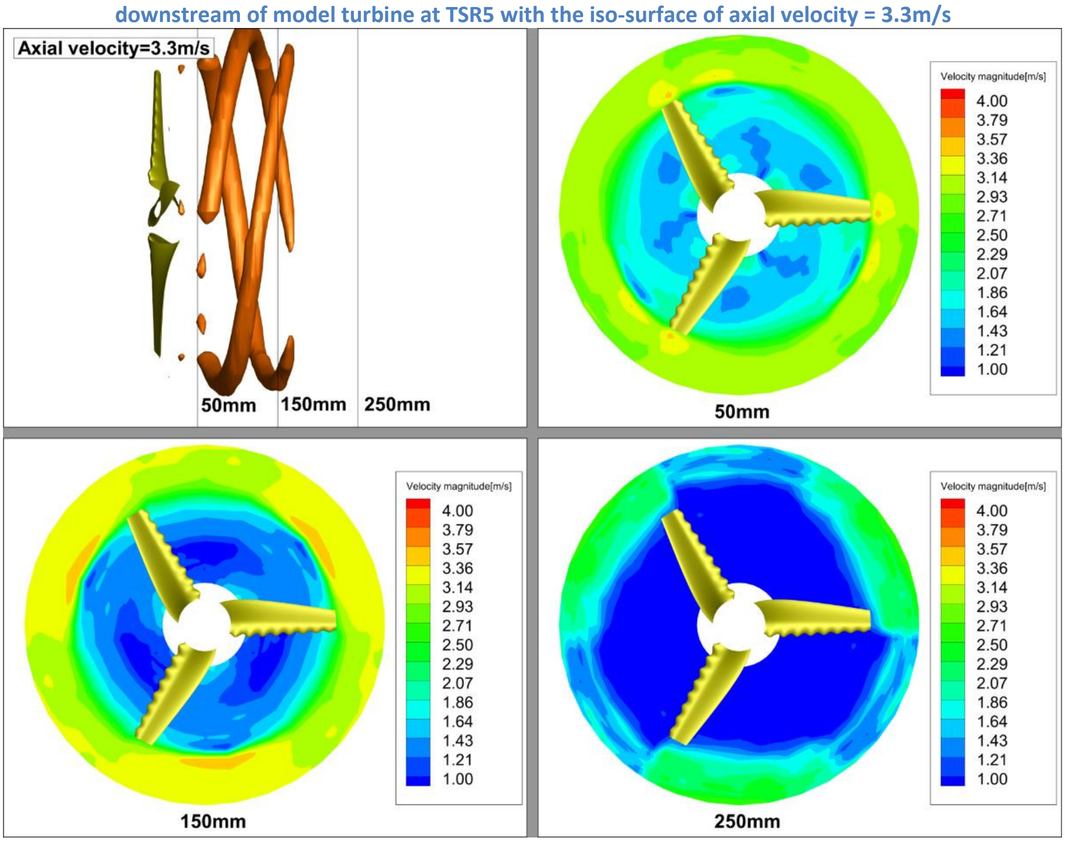

Figure 27. Velocity magnitude distribution for the Sin8 turbine at varied sections, 50mm, 150mm and 250mm the turbine at TSR5 with the iso-surface of axial velocity = 3.3m/s

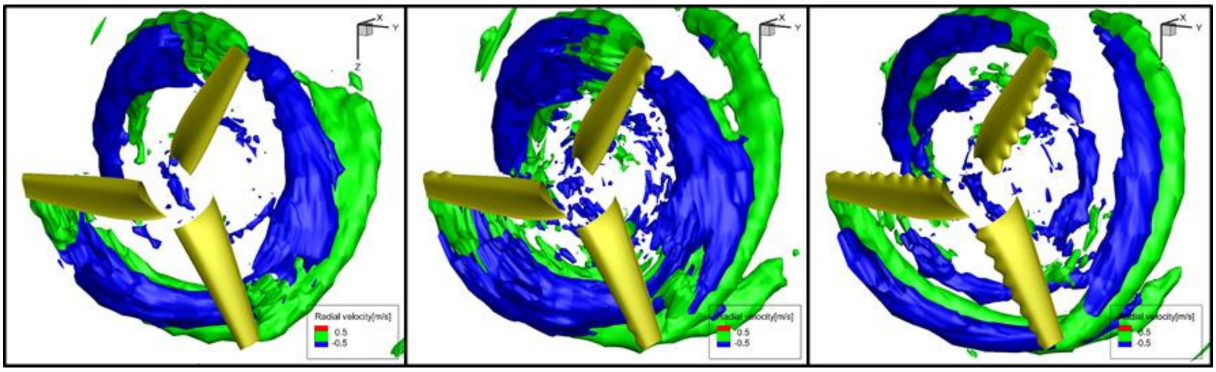

Figure 28. Iso-surface pair of radial velocity = +/-0.5m/s at TSR2 (Left: Ref; Middle: Sin2; Right: Sin8)

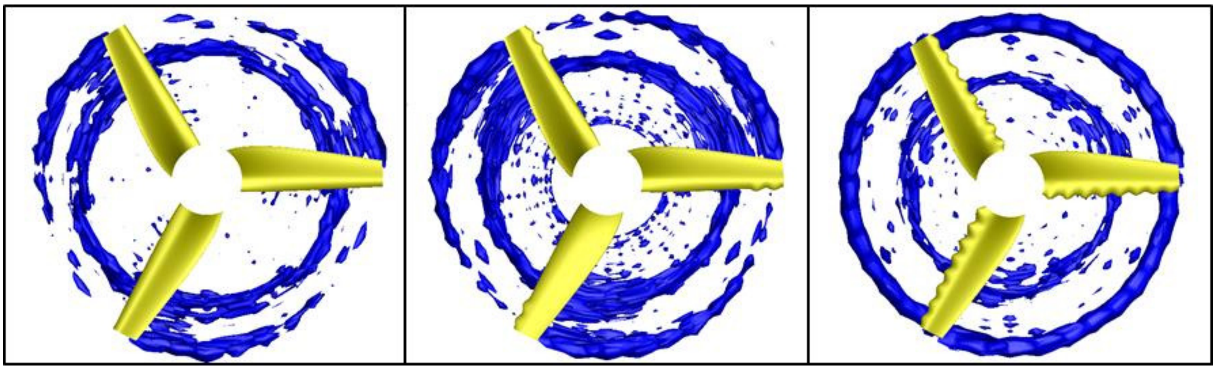

Figure 29. Iso-surface of vorticity (tangential) = 100 at TSR2 (Left: Ref; Middle: Sin2; Right: Sin8)

Table 1. Main particulars of tidal stream turbine model

r/R	0.2	0.3	0.4	0.5	0.6	0.7	0.8	0.9	1
Chord length(mm)	64.35	60.06	55.76	51.47	47.18	42.88	38.59	34.29	30
Pitch angle (deg)	27	15	7.5	4	2	0.5	-0.4	-1.3	-2
Hub radius (0.2R) = 40mm; Same section profile, S814, along the radial direction									

Table 2 Test matrix

V	TSR	RPM	Pitch angle	Tunnel pressure	Cav	Re
(m/s)			(º)	(mmhg)	(0.7r)	(0.7r)
2	0.5 ~ 8	47 ~ 763	0	850	48.534 ~ 1.684	0.76E+05 ~ 2.24E+05
2	0.5 ~ 8	47 ~ 763	+4	850	48.534 ~ 1.684	0.76E+05 ~ 2.24E+05
2	0.5 ~ 8	47 ~ 763	+8	850	48.534 ~ 1.684	0.76E+05 ~ 2.24E+05
3	0.5 ~ 8	71 ~ 1145	0	850	21.571 ~ 0.748	1.15E+05 ~ 3.36E+05
3	0.5 ~ 8	71 ~ 1145	+4	850	21.571 ~ 0.748	1.15E+05 ~ 3.36E+05
3	0.5 ~ 8	71 ~ 1145	+8	850	21.571 ~ 0.748	1.15E+05 ~ 3.36E+05
4	0.5 ~ 8	95 ~ 1527	0	850	12.134 ~ 0.421	1.53E+05 ~ 4.48E+05
4	0.5 ~ 8	95 ~ 1527	+4	850	12.134 ~ 0.421	1.53E+05 ~ 4.48E+05
4	0.5 ~ 8	95 ~ 1527	+8	850	12.134 ~ 0.421	1.53E+05 ~ 4.48E+05

Table 3. Technical specifications of Particle Image Velocity (PIV) system

Laser	NewWave Pegasus
Light sheet optics	80x70 high power Nd:YAG light sheet series
Synchronizer	NI PCI-6601 timer board
Camera	NanoSense MK III
Sensor size	1280x1024 pixels
Maximum capture frequency	1000Hz
Maximum images	3300
Calibration target	Multi-level 270x190 mm, 2^{nd} level -4
Seeding particles	Talisman 30 white 110 plastic powder

Table 4. Measured hydrodynamic performance data of model turbines in the selected PIV testing conditions

Power coefficient (Cp)					
Conditions	Ref	Sin2	(Increment ratio)	Sin8	(Increment ratio)
TSR2_4	17.1%	19.3%	12.4%	19.2%	12.1%
TSR4_3	46.4%	47.4%	2.2%	48.3%	4.3%
TSR5_3	44.4%	45.1%	1.6%	46.1%	4.0%
Thrust coefficient (C_T/10)					
Conditions	Ref	Sin2	(Increment ratio)	Sin8	(Increment ratio)
TSR2_4	6.0%	6.1%	1.4%	6.4%	6.4%
TSR4_3	8.6%	8.9%	4.6%	9.2%	7.7%
TSR5_3	8.6%	8.9%	4.0%	9.4%	9.2%

Table 5. 2D PIV measurement results of turbines at different radial positions (at TSR=2)

Ref_4_TSR2_1.0R	Sin2_4_TSR2_1.0R	Sin8_4_TSR2_1.0R
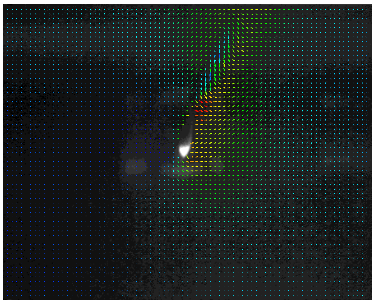	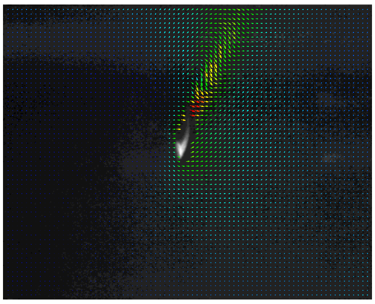	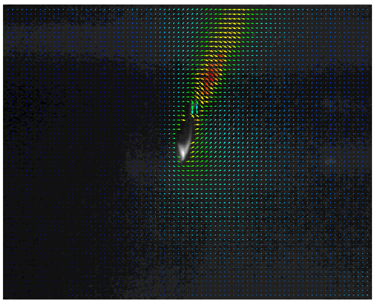
Ref_4_TSR2_0.95R	Sin2_4_TSR2_0.95R	Sin8_4_TSR2_0.95R
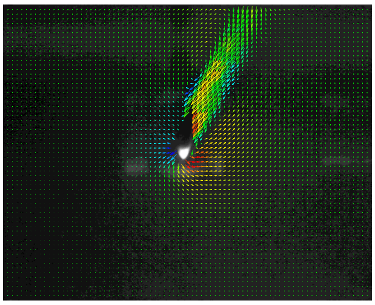	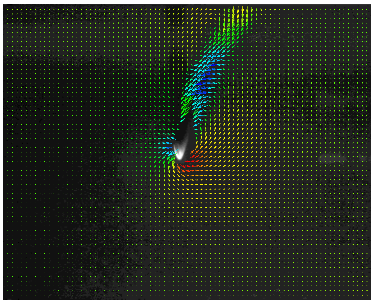	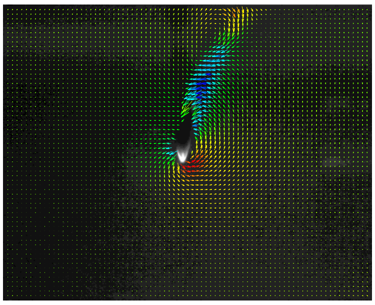
Ref_4_TSR2_0.9R	Sin2_4_TSR2_0.9R	Sin8_4_TSR2_0.9R
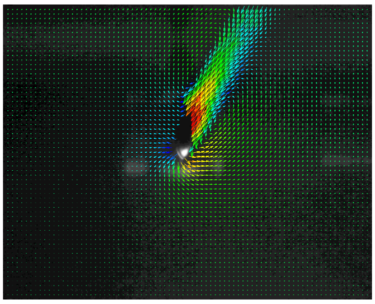	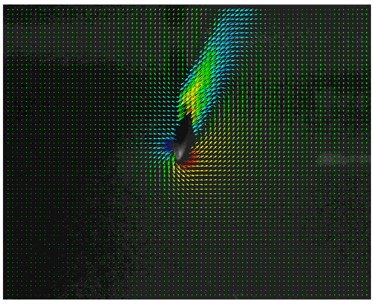	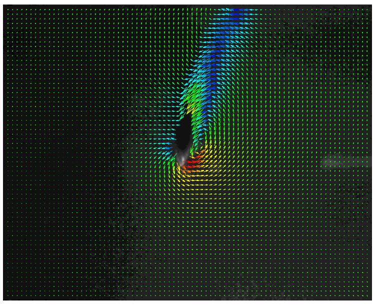
Ref_4_TSR2_0.85R	Sin2_4_TSR2_0.85R	Sin8_4_TSR2_0.85R
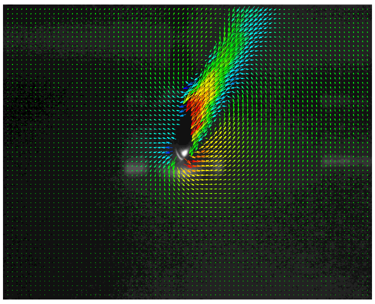	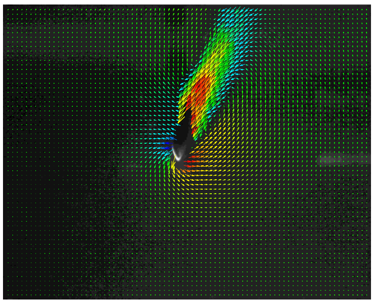	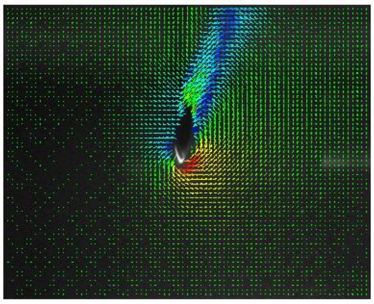
Ref_4_TSR2_0.8R	Sin2_4_TSR2_0.8R	Sin8_4_TSR2_0.8R
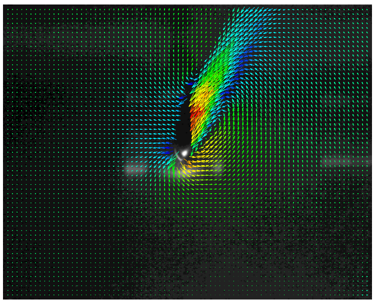	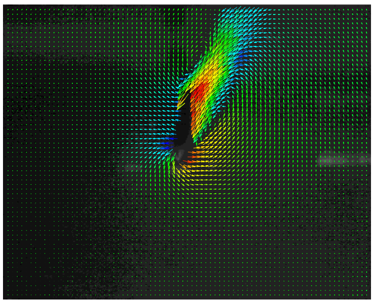	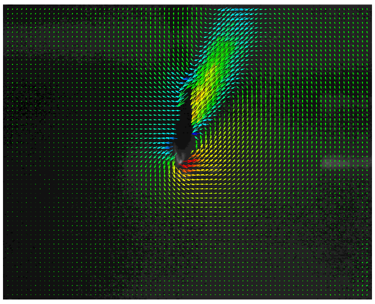

Ref_4_TSR2_0.75R

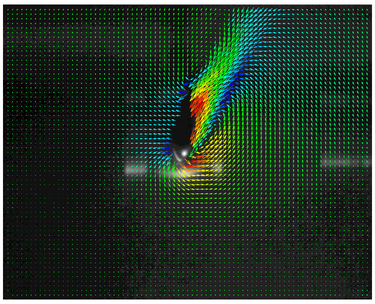

Sin2_4_TSR2_0.75R

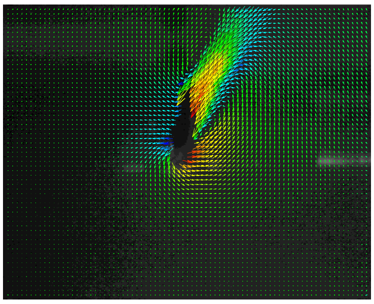

Sin8_4_TSR2_0.75R

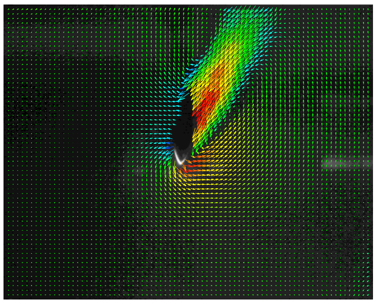

Ref_4_TSR2_0.7R

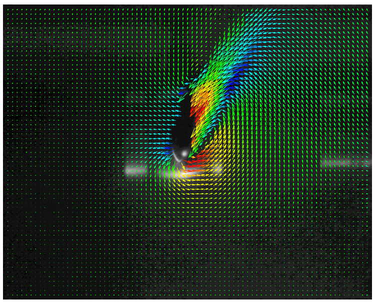

Sin2_4_TSR2_0.7R

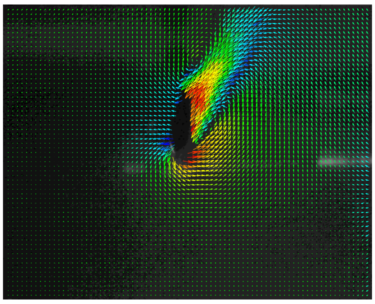

Sin8_4_TSR2_0.7R

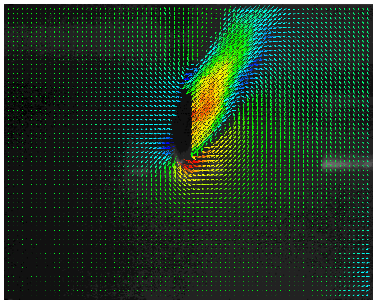

Ref_4_TSR2_0.65R

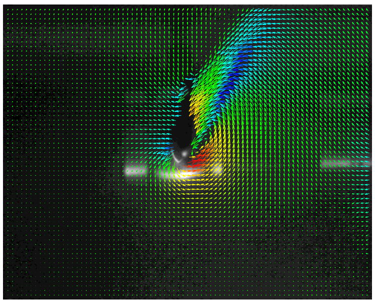

Sin2_4_TSR2_0.65R

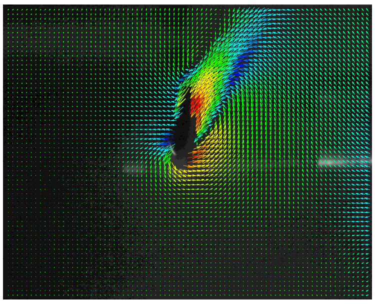

Sin8_4_TSR2_0.65R

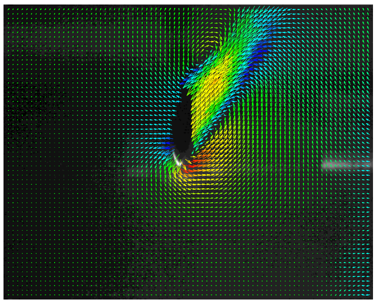

Ref_4_TSR2_0.6R

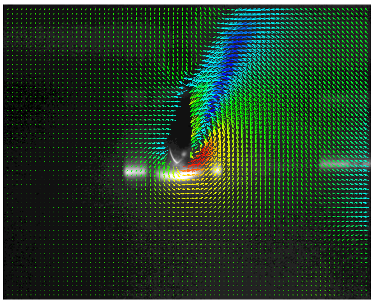

Sin2_4_TSR2_0.6R

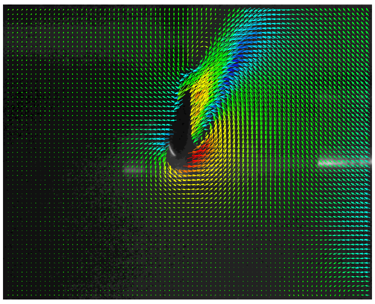

Sin8_4_TSR2_0.6R

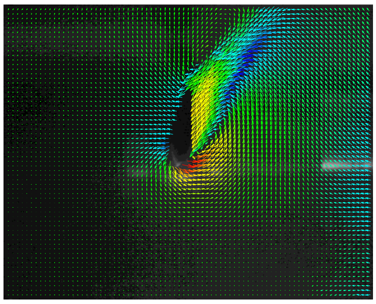

Ref_4_TSR2_0.55R

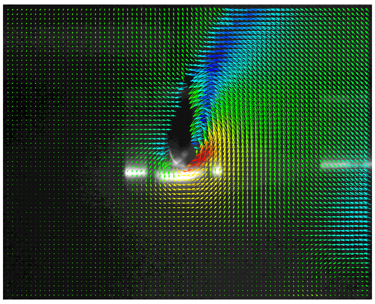

Sin2_4_TSR2_0.55R

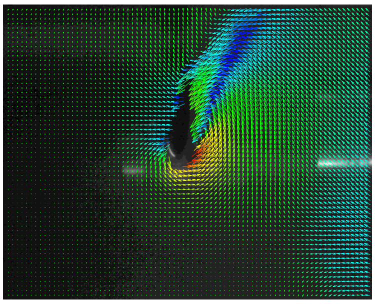

Sin8_4_TSR2_0.55R

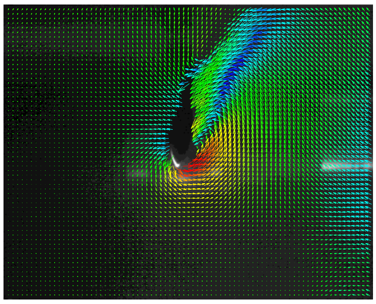

Ref_4_TSR2_0.5R

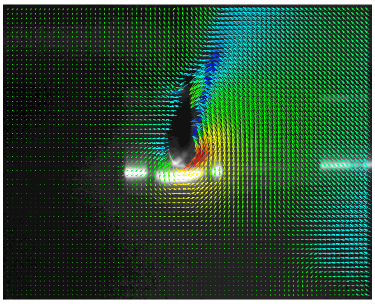

Sin2_4_TSR2_0.5R

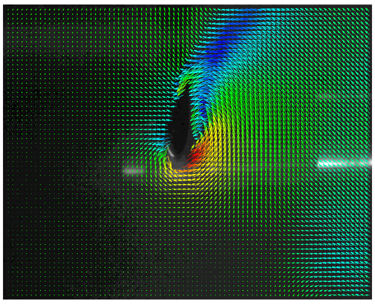

Sin8_4_TSR2_0.5R

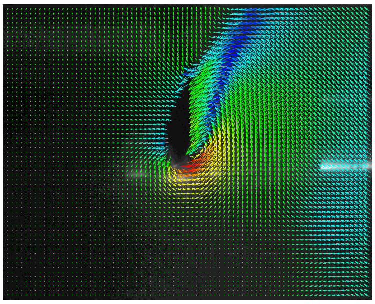

Ref_4_TSR2_0.45R

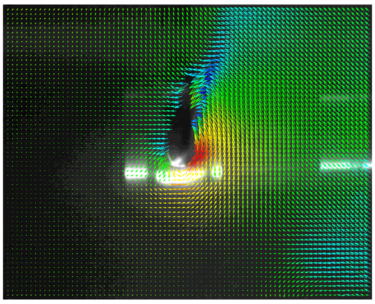

Sin2_4_TSR2_0.45R

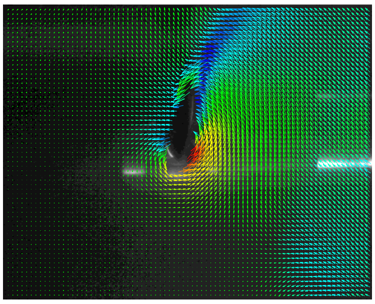

Sin8_4_TSR2_0.45R

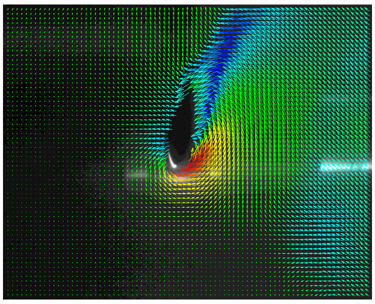

Ref_4_TSR2_0.4R

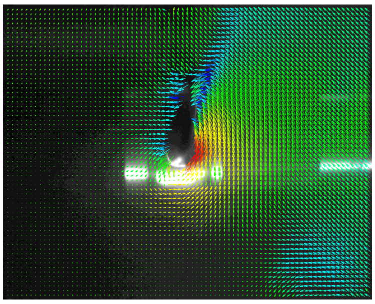

Sin2_4_TSR2_0.4R

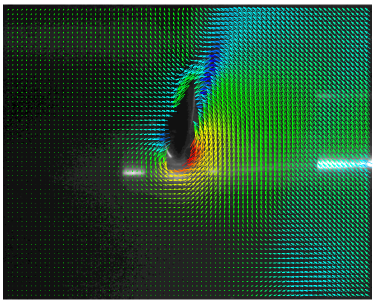

Sin8_4_TSR2_0.4R

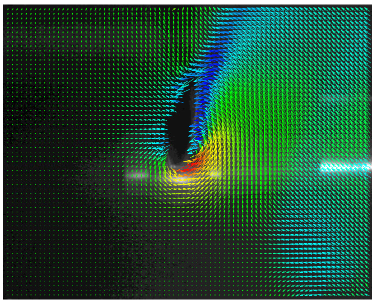

Ref_4_TSR2_0.35R

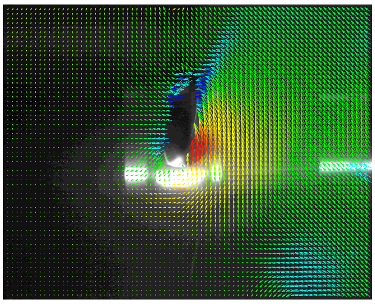

Sin2_4_TSR2_0.35R

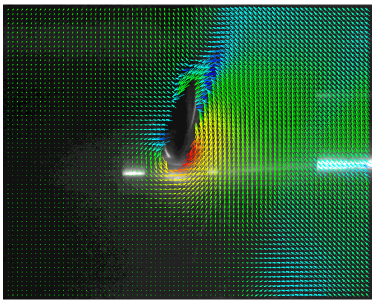

Sin8_4_TSR2_0.35R

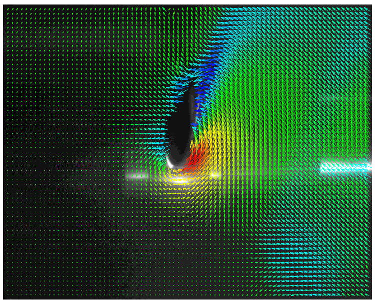

Ref_4_TSR2_0.3R

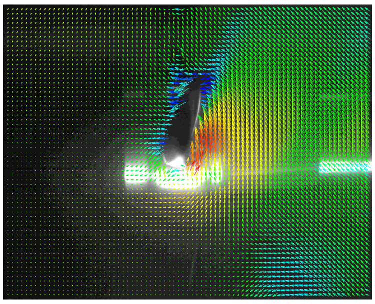

Sin2_4_TSR2_0.3R

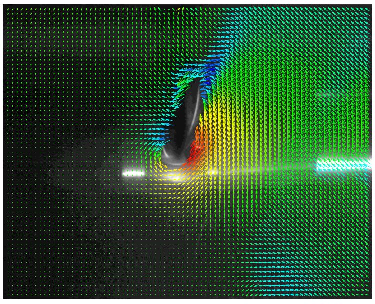

Sin8_4_TSR2_0.3R

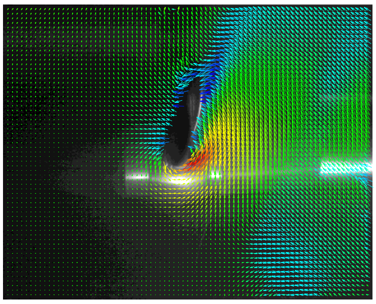

Ref_4_TSR2_0.25R	Sin2_4_TSR2_0.25R	Sin8_4_TSR2_0.25R
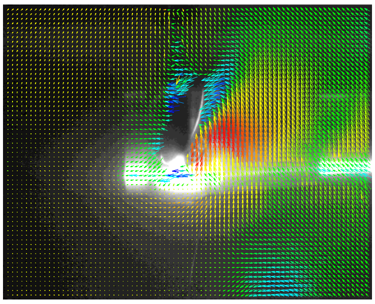	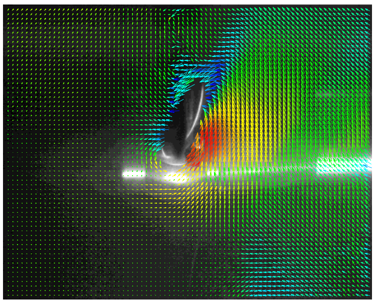	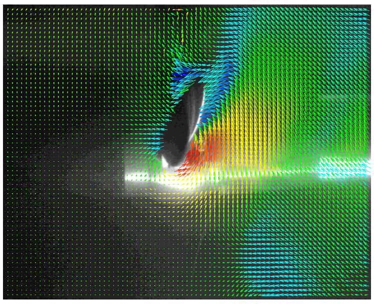

Table 6. Vorticity Z distribution of turbines at different radial positions (at TSR=2)

Z Vorticity: 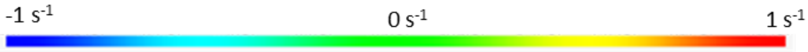

Ref_4_TSR2_1.0R	Sin2_4_TSR2_1.0R	Sin8_4_TSR2_1.0R
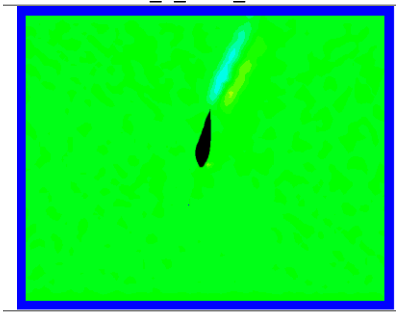	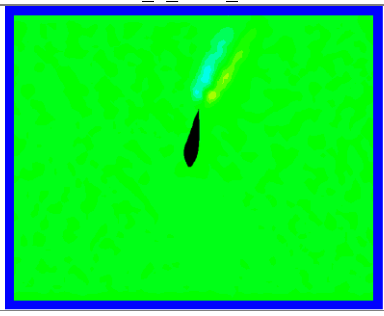	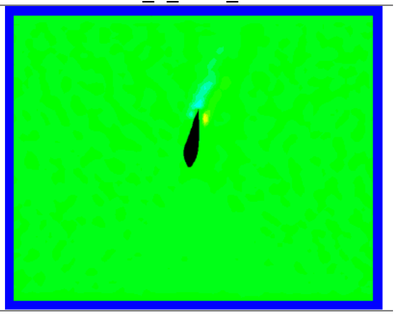
Ref_4_TSR2_0.95R	Sin2_4_TSR2_0.95R	Sin8_4_TSR2_0.95R
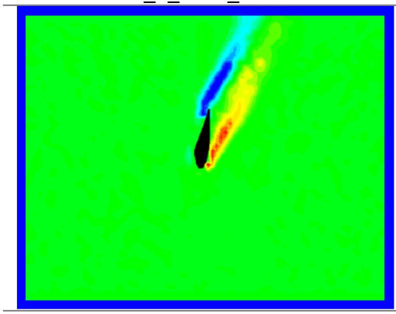	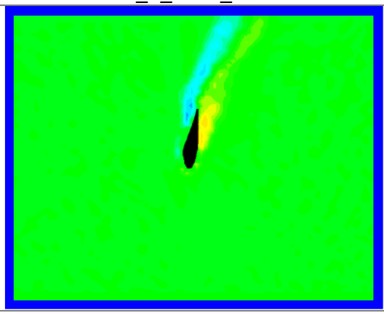	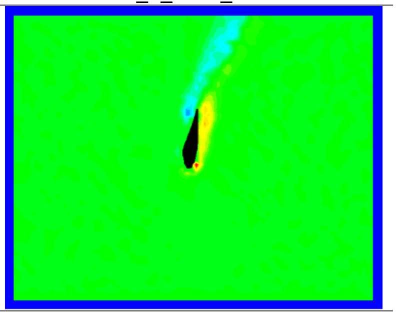
Ref_4_TSR2_0.9R	Sin2_4_TSR2_0.9R	Sin8_4_TSR2_0.9R
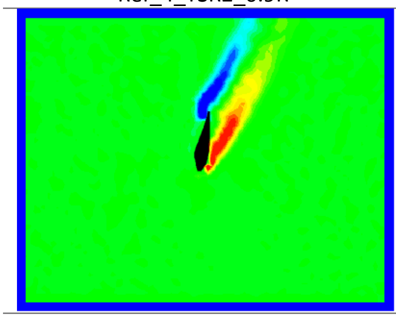	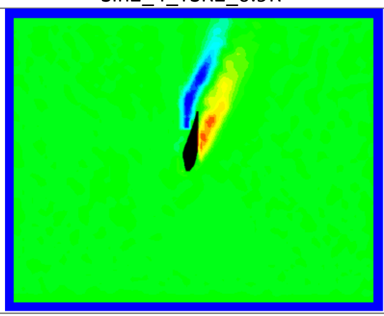	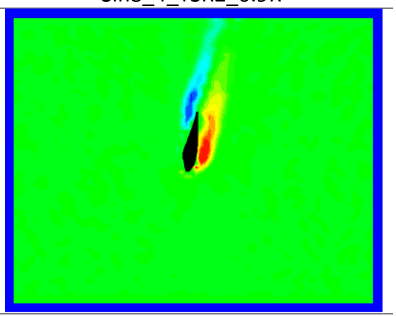
Ref_4_TSR2_0.85R	Sin2_4_TSR2_0.85R	Sin8_4_TSR2_0.85R
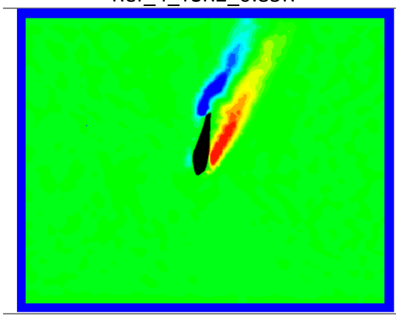	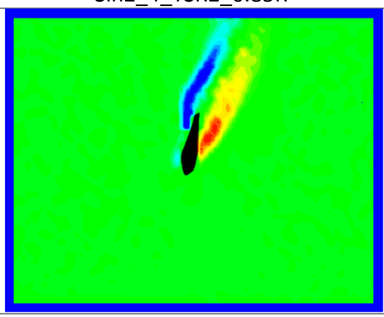	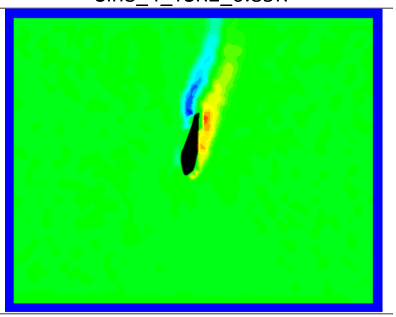
Ref_4_TSR2_0.8R	Sin2_4_TSR2_0.8R	Sin8_4_TSR2_0.8R
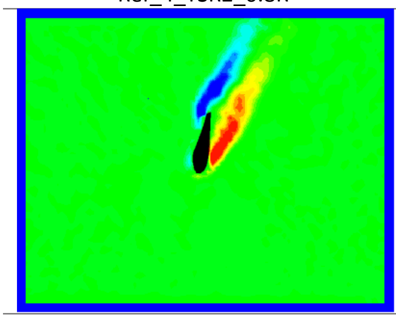	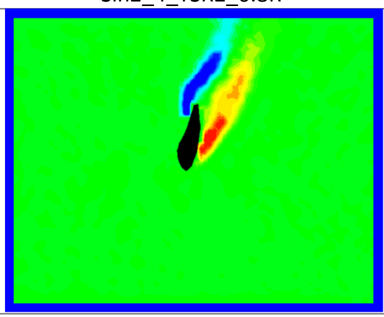	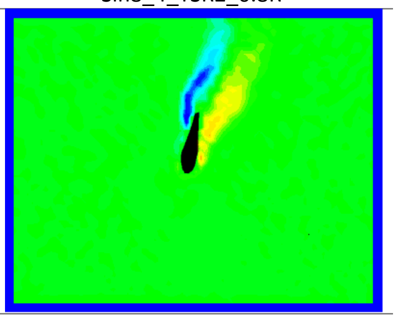

Ref_4_TSR2_0.75R	Sin2_4_TSR2_0.75R	Sin8_4_TSR2_0.75R
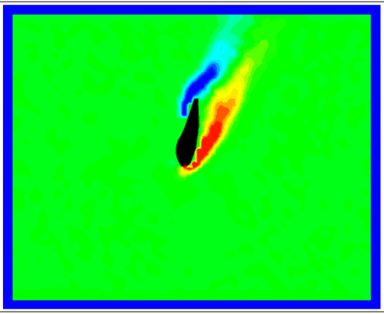	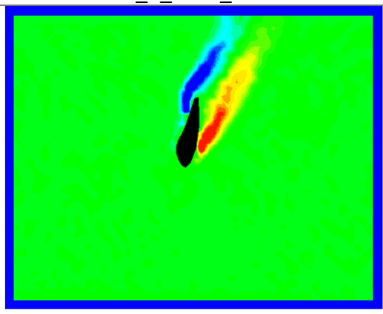	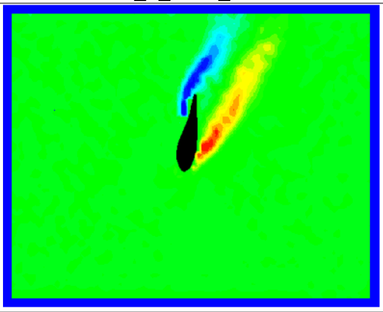
Ref_4_TSR2_0.7R	Sin2_4_TSR2_0.7R	Sin8_4_TSR2_0.7R
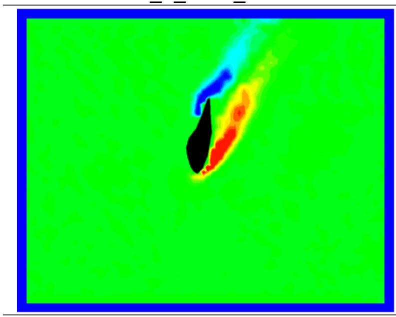	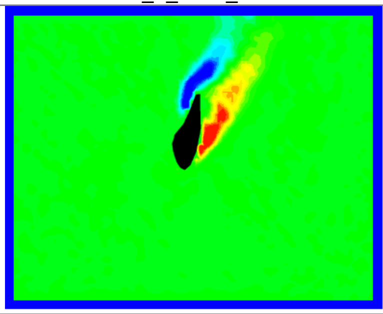	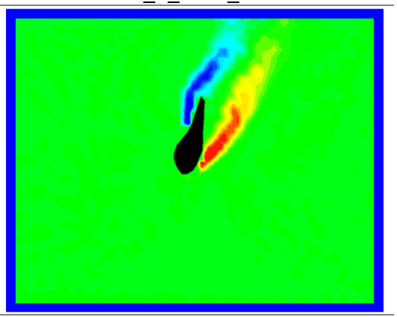
Ref_4_TSR2_0.65R	Sin2_4_TSR2_0.65R	Sin8_4_TSR2_0.65R
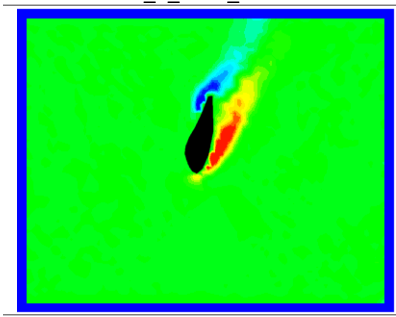	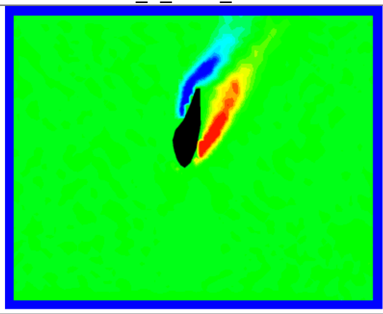	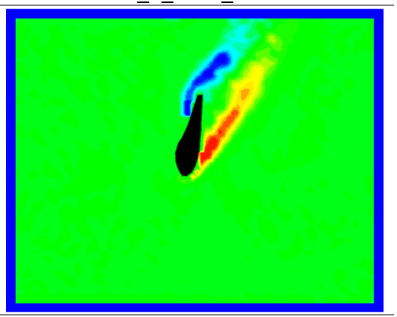
Ref_4_TSR2_0.6R	Sin2_4_TSR2_0.6R	Sin8_4_TSR2_0.6rR
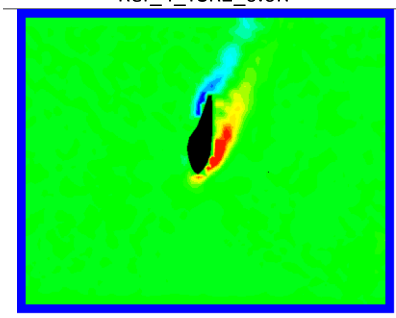	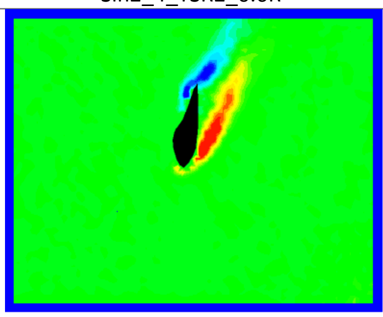	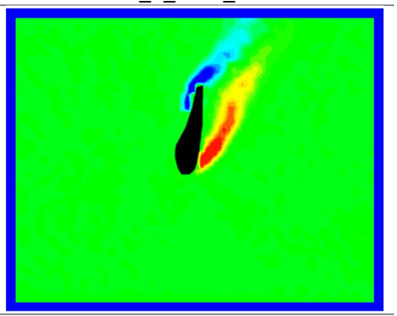
Ref_4_TSR2_0.55R	Sin2_4_TSR2_0.55R	Sin8_4_TSR2_0.55R
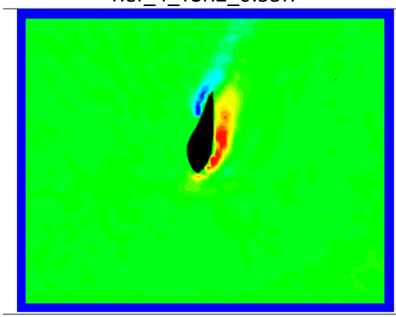	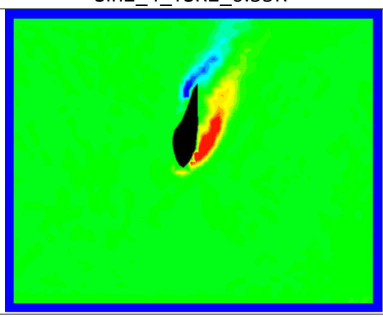	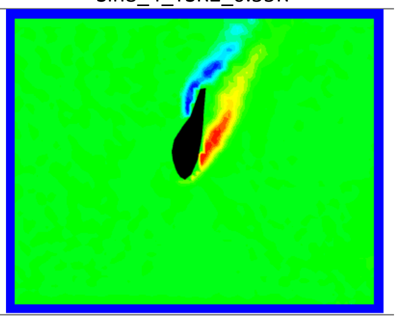

Ref_4_TSR2_0.5R	Sin2_4_TSR2_0.5R	Sin8_4_TSR2_0.5R
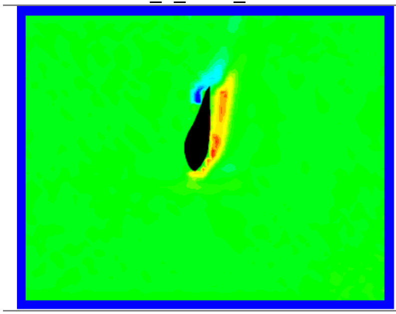	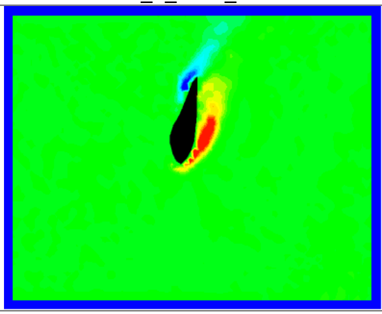	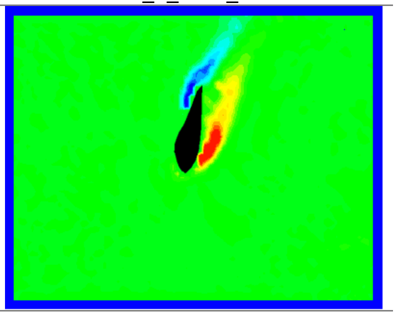
Ref_4_TSR2_0.45R	Sin2_4_TSR2_0.45R	Sin8_4_TSR2_0.45R
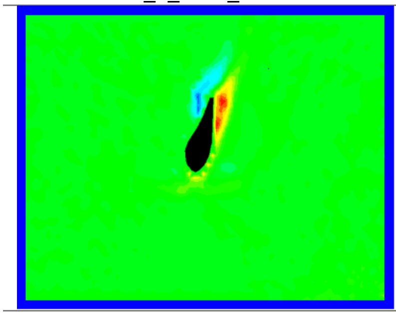	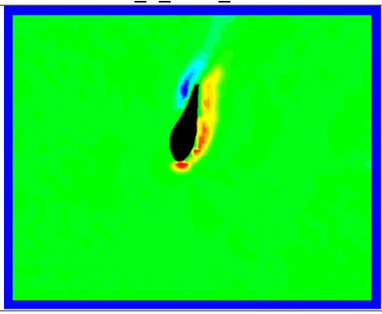	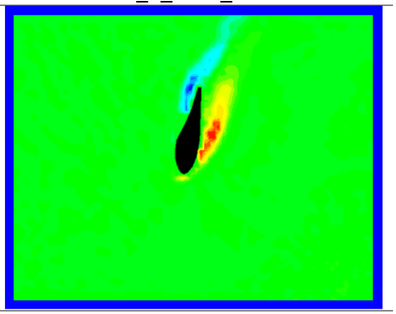
Ref_4_TSR2_0.4R	Sin2_4_TSR2_0.4R	Sin8_4_TSR2_0.4R
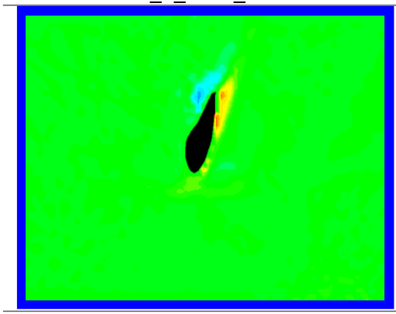	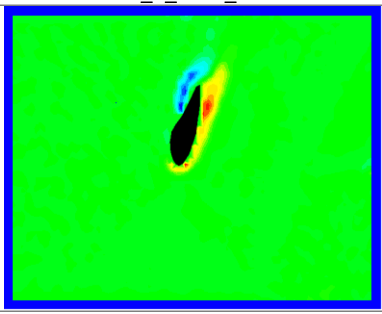	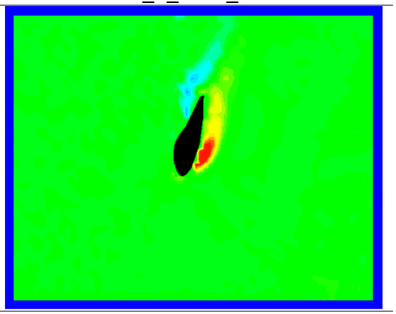
Ref_4_TSR2_0.35R	Sin2_4_TSR2_0.35R	Sin8_4_TSR2_0.35R
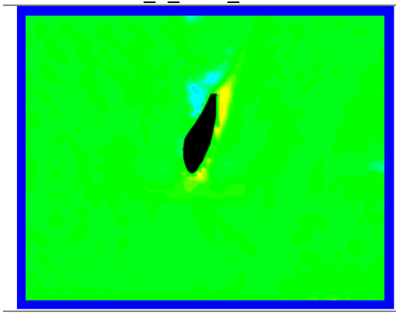	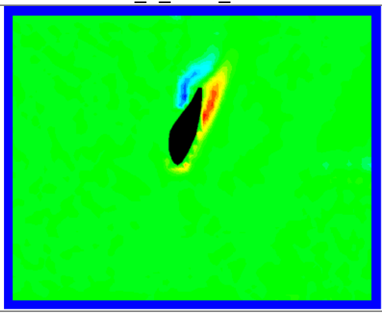	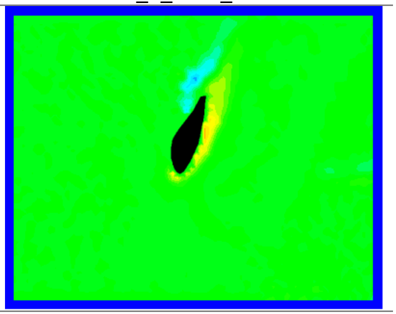
Ref_4_TSR2_0.3R	Sin2_4_TSR2_0.3R	Sin8_4_TSR2_0.3R
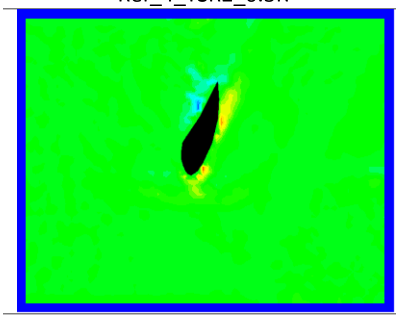	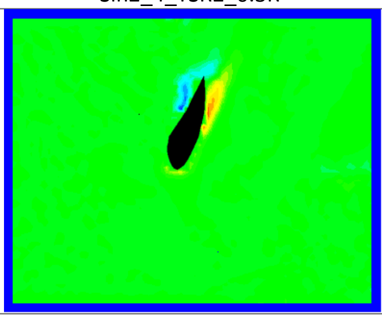	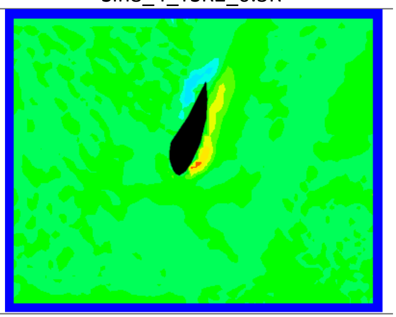

Ref_4_TSR2_0.25R	Sin2_4_TSR2_0.25R	Sin8_4_TSR2_0.25R
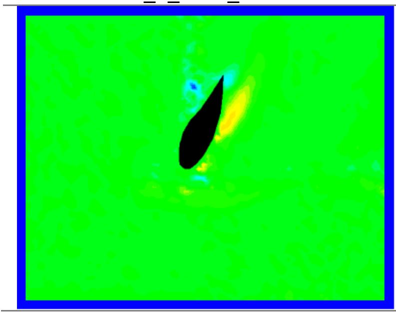	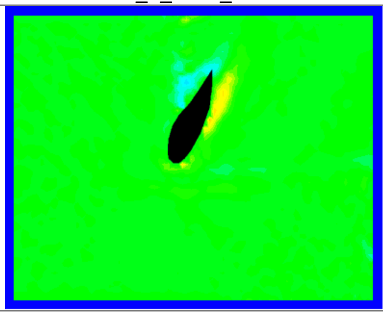	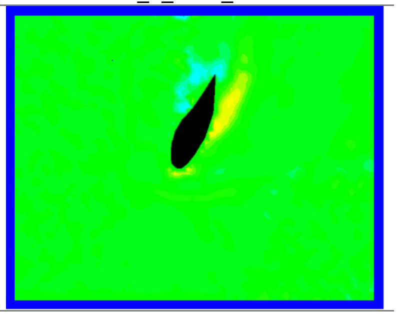

Appendix A:

The database of PIV measurement of flow separation under TSR4 and TSR5 has been presented as follow in Table 7 and Table 8 respectively.

Table 7 2D PIV measurement results of turbines at different radial positions (at TSR=4)

Ref_3_TSR4_1.0R	Sin2_3_TSR4_1.0R	Sin8_3_TSR4_1.0R
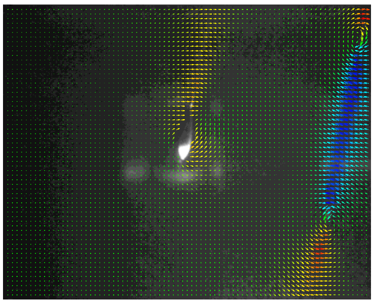	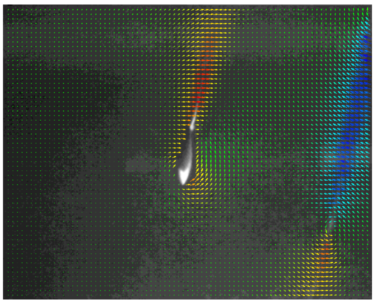	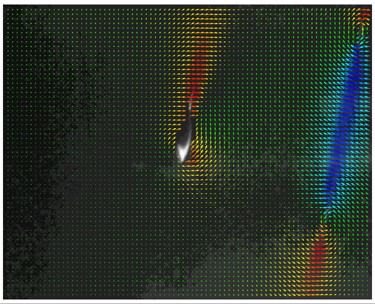
Ref_3_TSR4_0.95R	Sin2_3_TSR4_0.95R	Sin8_3_TSR4_0.95R
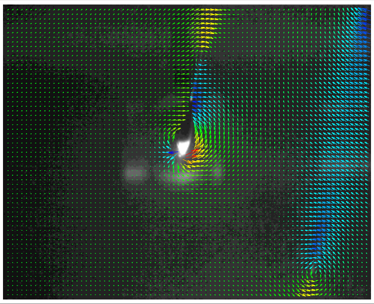	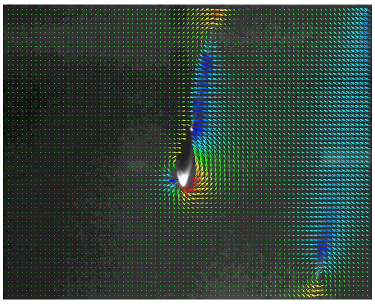	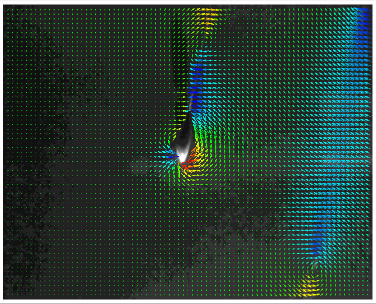
Ref_3_TSR4_0.9R	Sin2_3_TSR4_0.9R	Sin8_3_TSR4_0.9R
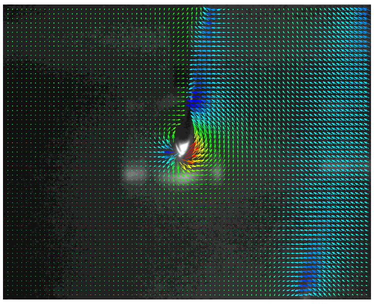	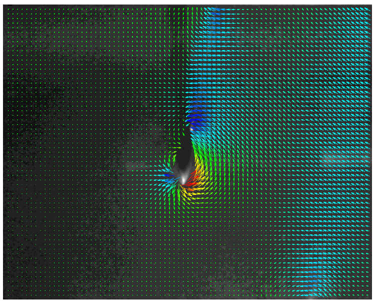	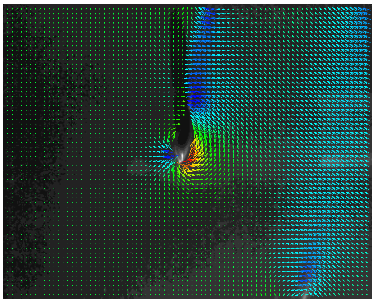
Ref_3_TSR4_0.85R	Sin2_3_TSR4_0.85R	Sin8_3_TSR4_0.85R
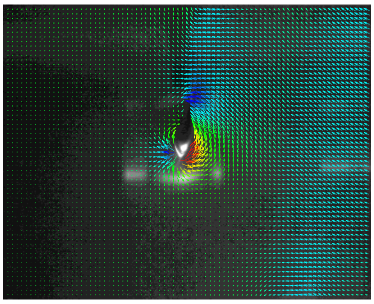	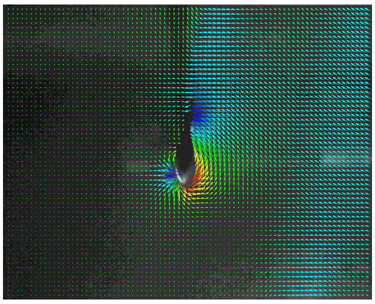	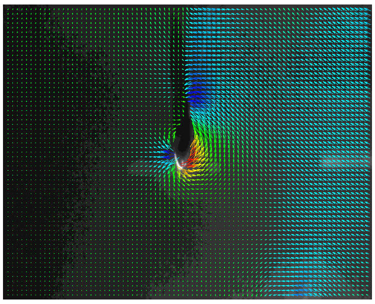

Ref_3_TSR4_0.8R	Sin2_3_TSR4_0.8R	Sin8_3_TSR4_0.8R
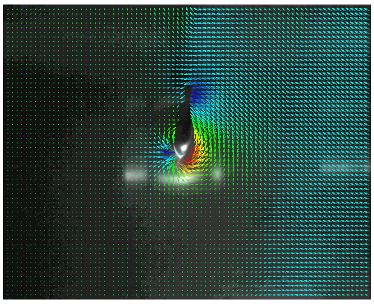	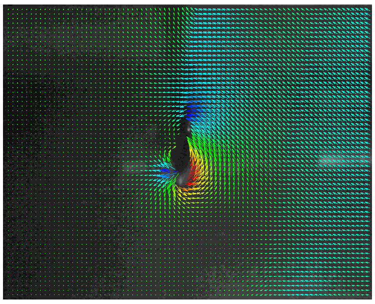	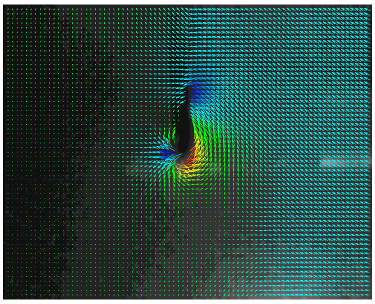
Ref_3_TSR4_0.75R	Sin2_3_TSR4_0.75R	Sin8_3_TSR4_0.75R
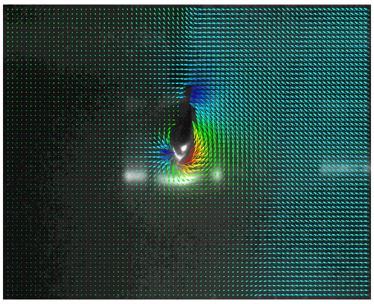	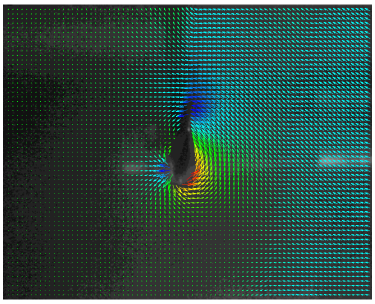	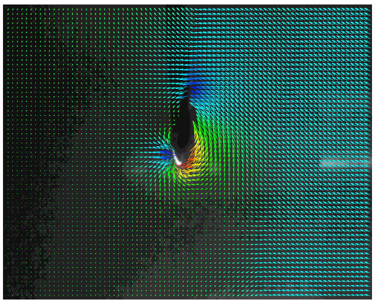
Ref_3_TSR4_0.7R	Sin2_3_TSR4_0.7R	Sin8_3_TSR4_0.7R
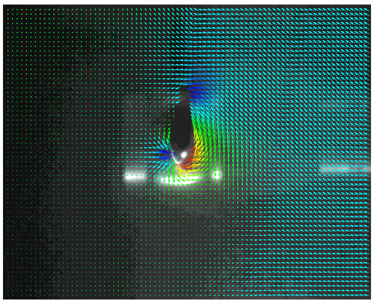	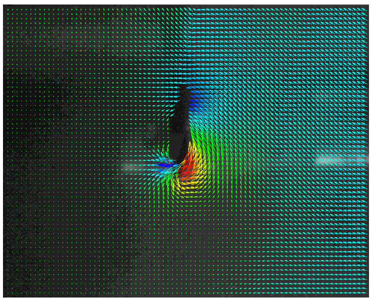	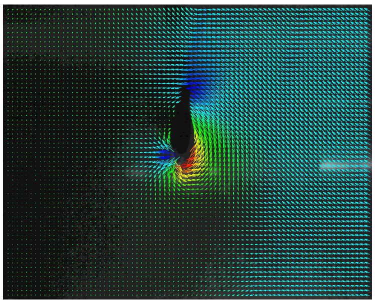
Ref_3_TSR4_0.65R	Sin2_3_TSR4_0.65R	Sin8_3_TSR4_0.65R
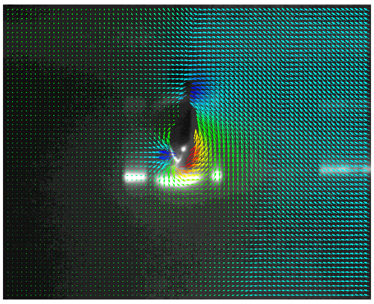	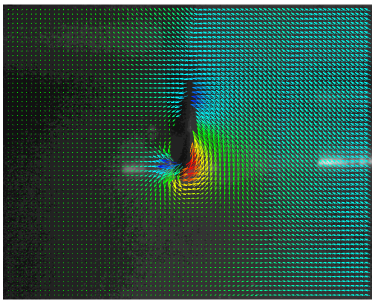	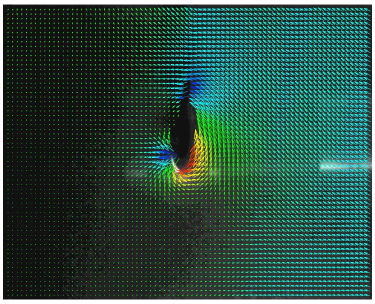
Ref_3_TSR4_0.6R	Sin2_3_TSR4_0.6R	Sin8_3_TSR4_0.6R
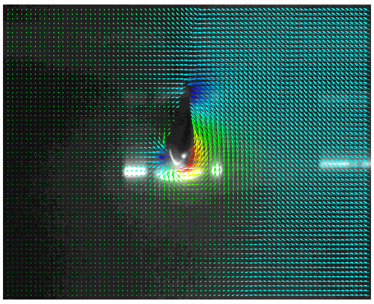	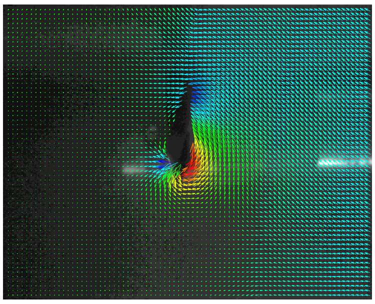	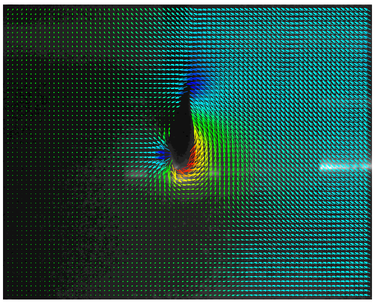

Ref_3_TSR4_0.55R	Sin2_3_TSR4_0.55R	Sin8_3_TSR4_0.55R
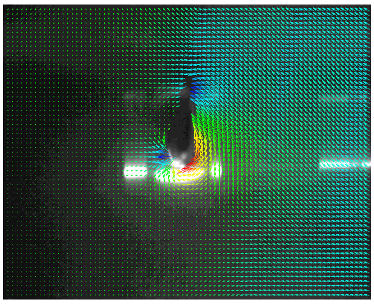	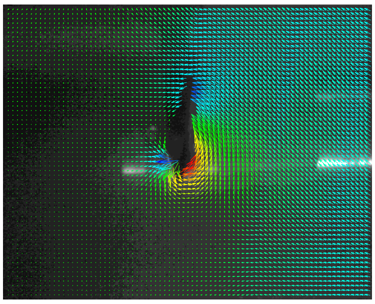	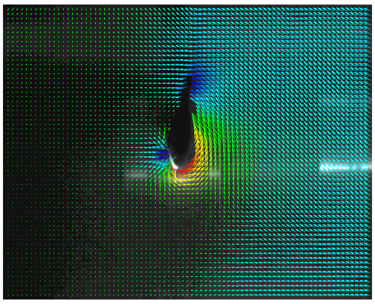
Ref_3_TSR4_0.5R	Sin2_3_TSR4_0.5R	Sin8_3_TSR4_0.5R
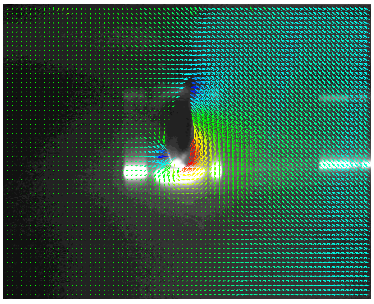	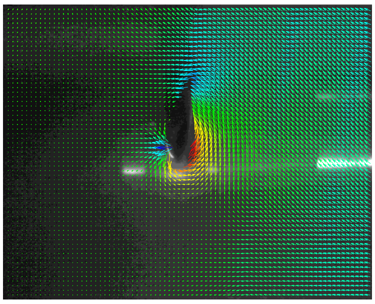	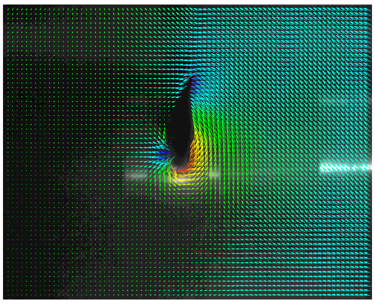
Ref_3_TSR4_0.45R	Sin2_3_TSR4_0.45R	Sin8_3_TSR4_0.45R
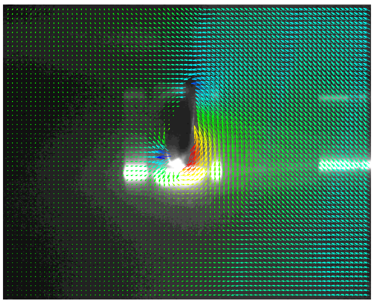	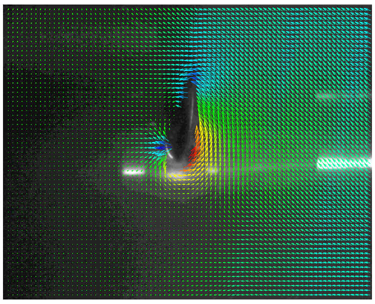	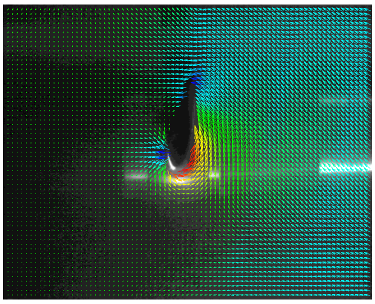
Ref_3_TSR4_0.4R	Sin2_3_TSR4_0.4R	Sin8_3_TSR4_0.4R
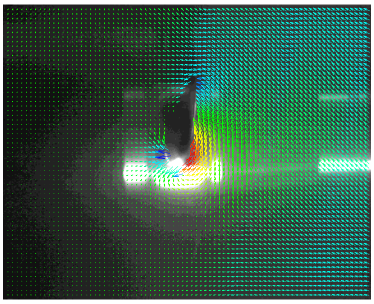	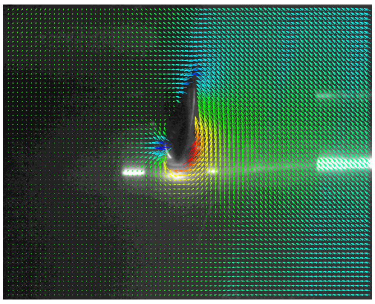	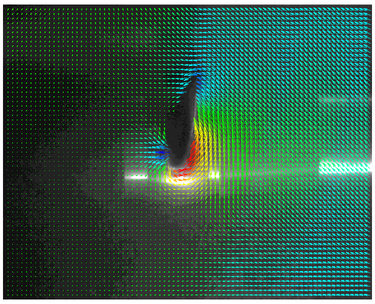
Ref_3_TSR4_0.35R	Sin2_3_TSR4_0.35R	Sin8_3_TSR4_0.35R
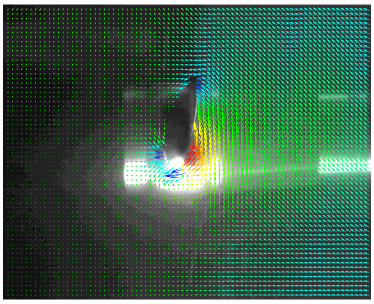	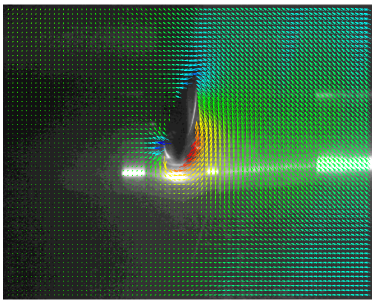	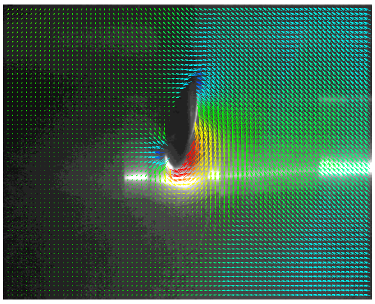

Ref_3_TSR4_0.3R	Sin2_3_TSR4_0.3R	Sin8_3_TSR4_0.3R
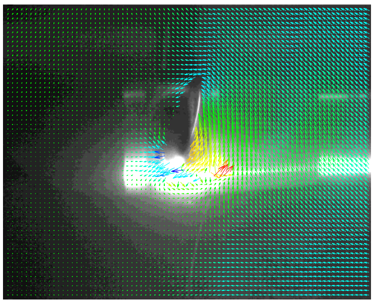	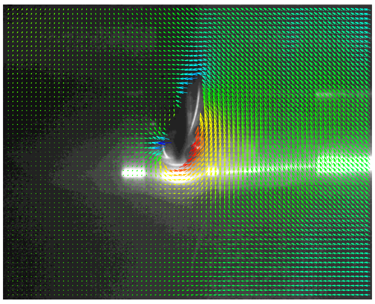	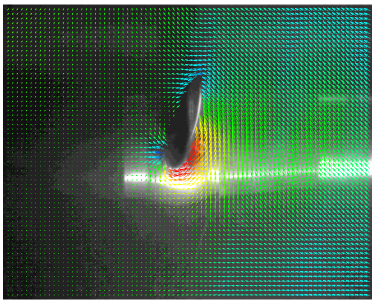
Ref_3_TSR4_0.25R	Sin2_3_TSR4_0.25R	Sin8_3_TSR4_0.25R
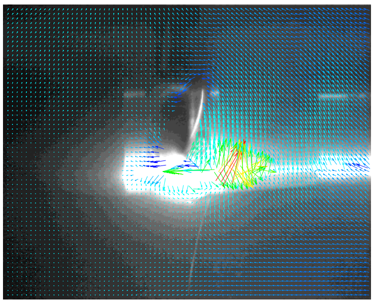	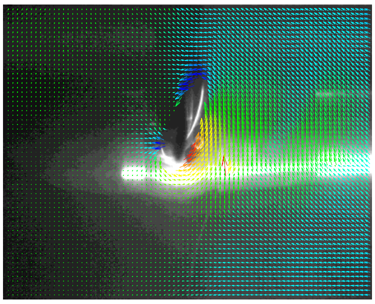	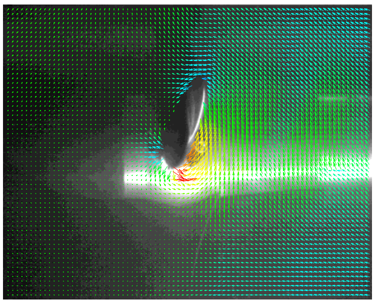

Table 8. 2D PIV measurement results of turbines at different radial positions (at TSR=5)

Ref_3_TSR5_1.0R	Sin2_3_TSR5_1.0R	Sin8_3_TSR5_1.0R
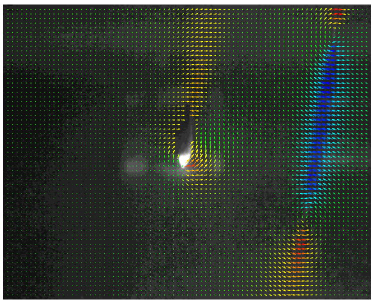	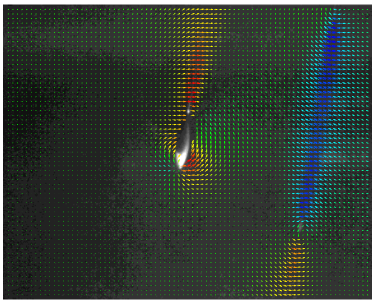	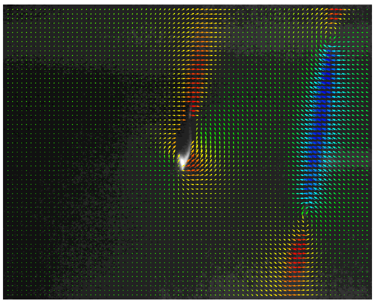
Ref_3_TSR5_0.95R	Sin2_3_TSR5_0.95R	Sin8_3_TSR5_0.95R
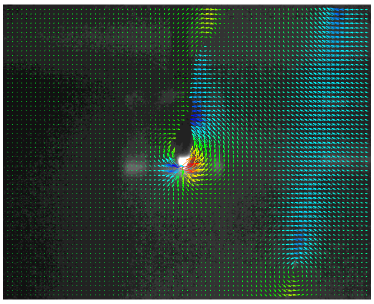	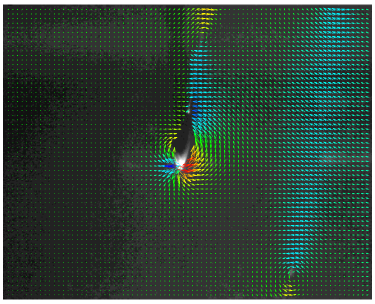	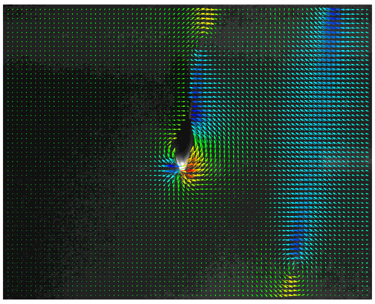
Ref_3_TSR5_0.9R	Sin2_3_TSR5_0.9R	Sin8_3_TSR5_0.9R
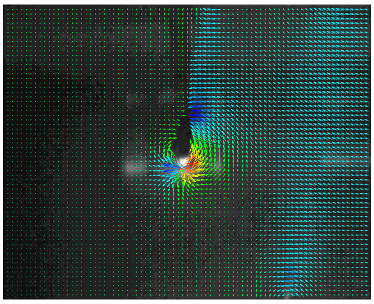	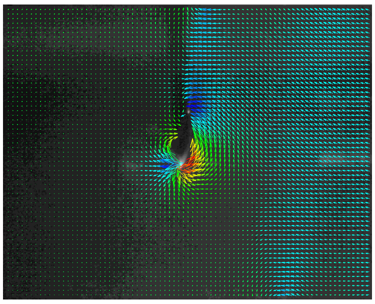	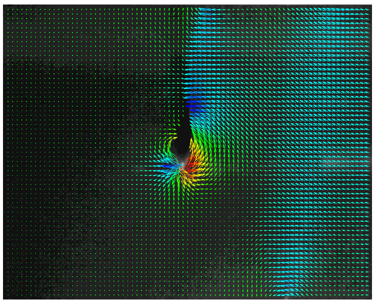
Ref_3_TSR5_0.85R	Sin2_3_TSR5_0.85R	Sin8_3_TSR5_0.85R
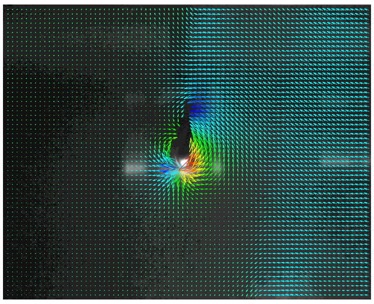	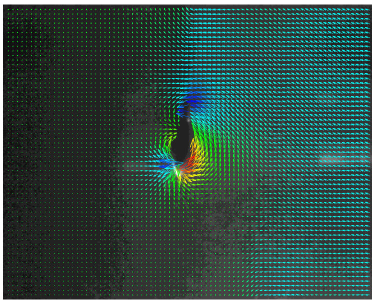	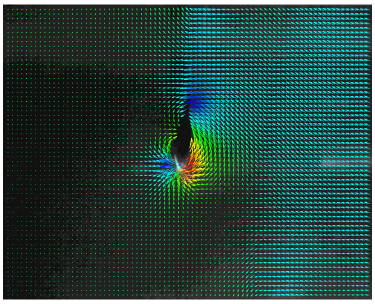
Ref_3_TSR5_0.8R	Sin2_3_TSR5_0.8R	Sin8_3_TSR5_0.8R
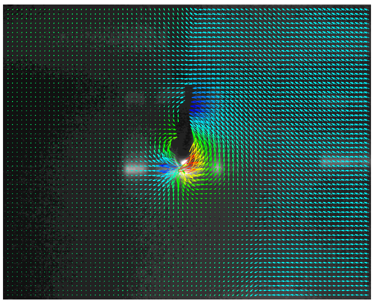	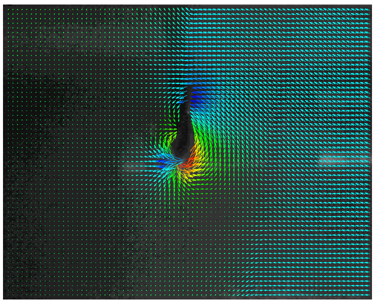	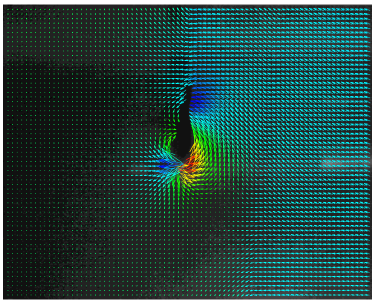

Ref_3_TSR5_0.75R	Sin2_3_TSR5_0.75R	Sin8_3_TSR5_0.75R
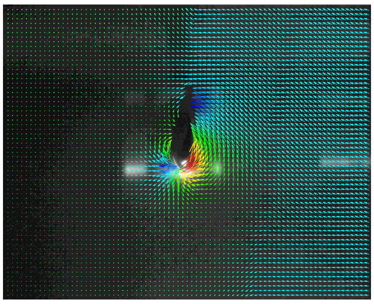	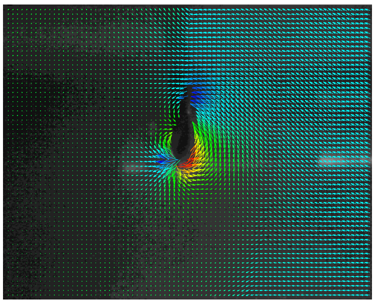	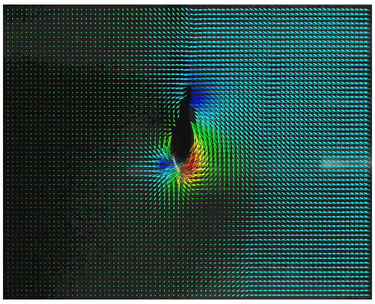
Ref_3_TSR5_0.7R	Sin2_3_TSR5_0.7R	Sin8_3_TSR5_0.7R
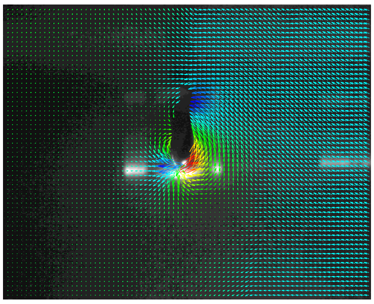	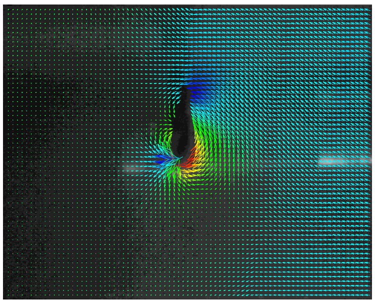	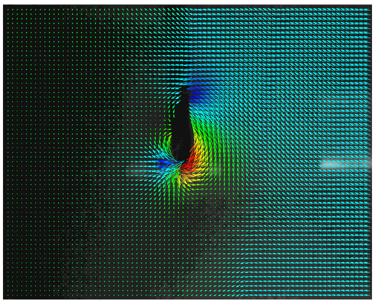
Ref_3_TSR5_0.65R	Sin2_3_TSR5_0.65R	Sin8_3_TSR5_0.65R
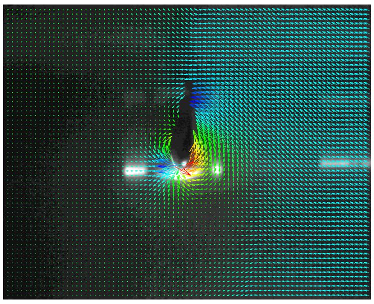	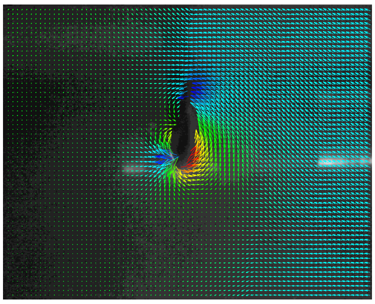	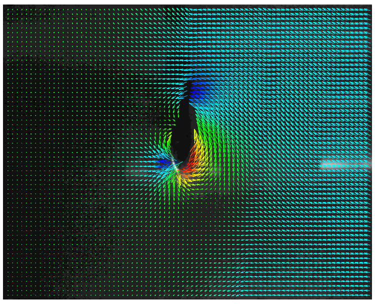
Ref_3_TSR5_0.6R	Sin2_3_TSR5_0.6R	Sin8_3_TSR5_0.6R
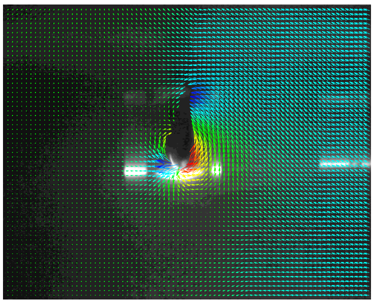	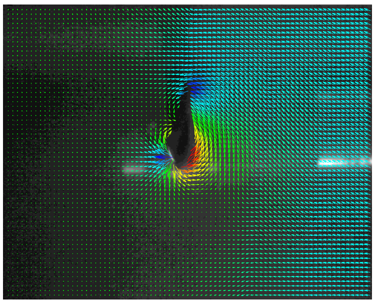	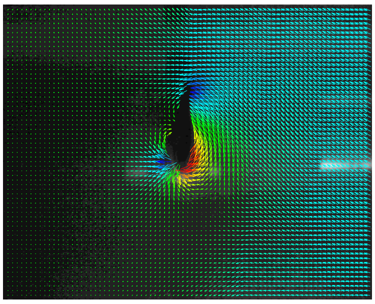
Ref_3_TSR5_0.55R	Sin2_3_TSR5_0.55R	Sin8_3_TSR5_0.55R
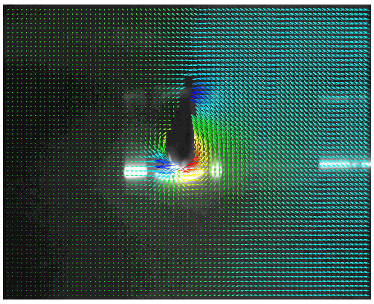	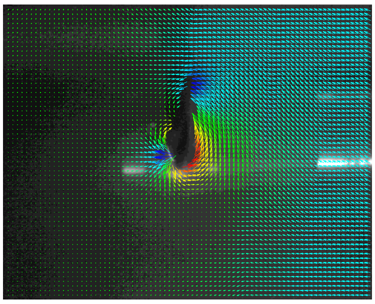	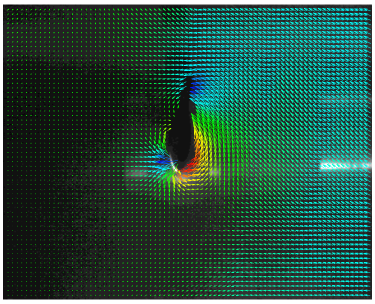

Ref_3_TSR5_0.5R	Sin2_3_TSR5_0.5R	Sin8_3_TSR5_0.5R
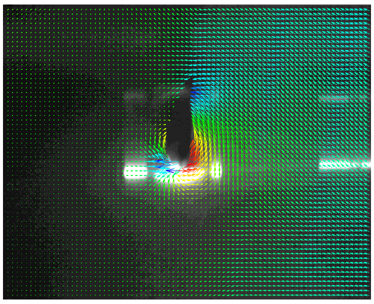	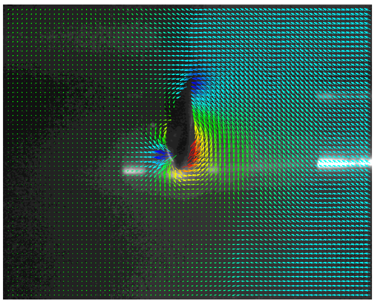	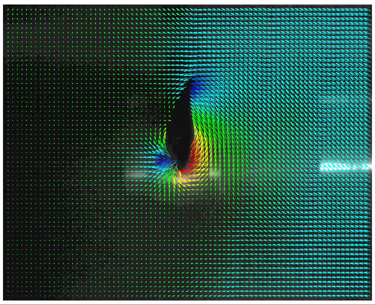
Ref_3_TSR5_0.45R	Sin2_3_TSR5_0.45R	Sin8_3_TSR5_0.45R
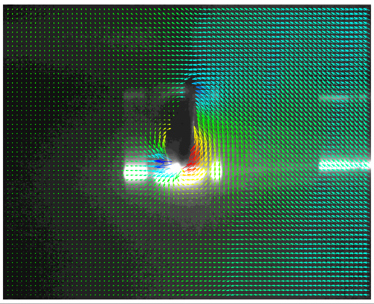	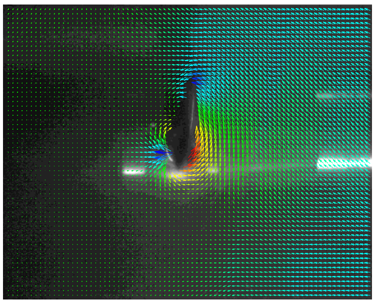	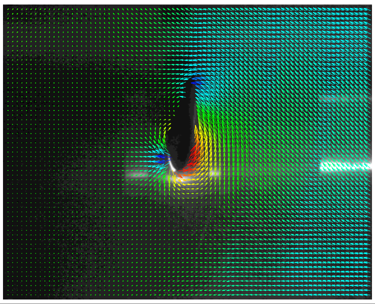
Ref_3_TSR5_0.4R	Sin2_3_TSR5_0.4R	Sin8_3_TSR5_0.4R
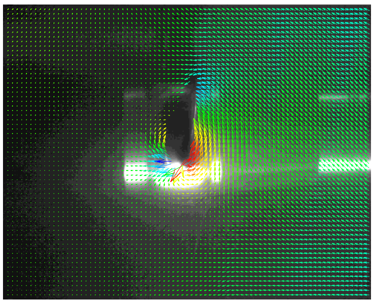	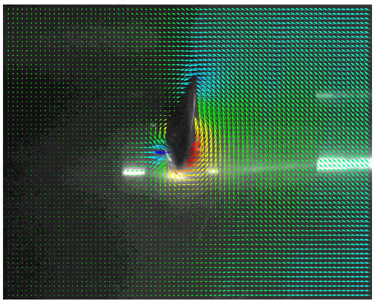	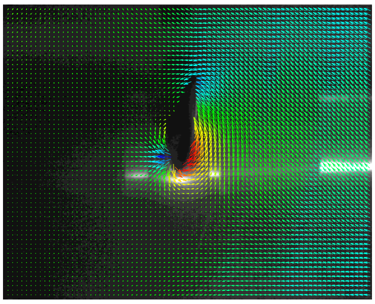
Ref_3_TSR5_0.35R	Sin2_3_TSR5_0.35R	Sin8_3_TSR5_0.35R
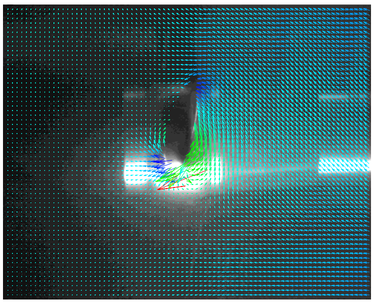	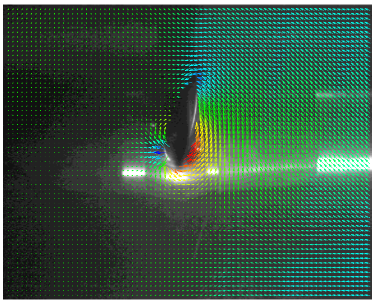	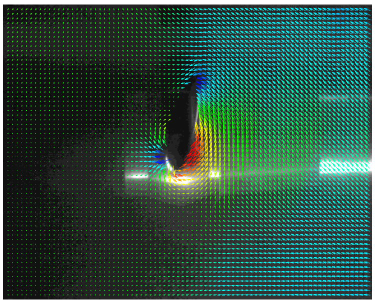
Ref_3_TSR5_0.3R	Sin2_3_TSR5_0.3R	Sin8_3_TSR5_0.3R
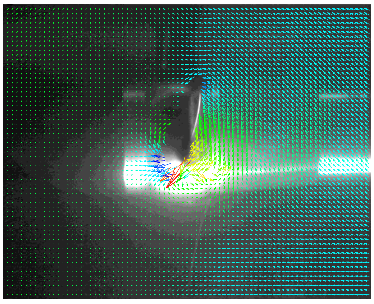	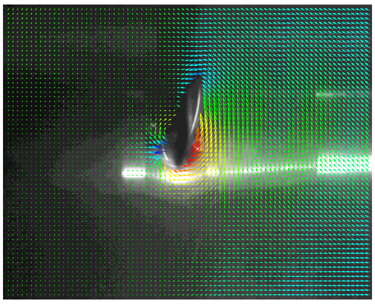	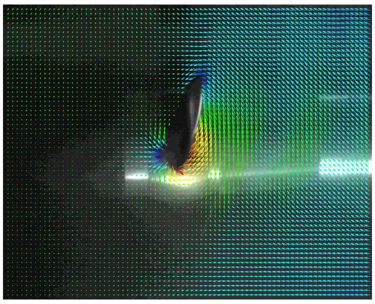

Ref_3_TSR5_0.25R	Sin2_3_TSR5_0.25R	Sin8_3_TSR5_0.25R